DEVELOPMENT OF SURFACE-MOUNTED SMART PIEZOELECTRIC MODULES FOR CONDITION ASSESSMENT OF BRIDGES

FINAL PROJECT REPORT

By

Pizhong Qiao, Ph.D., P.E., Professor
Ayumi K. Manawadu, Ph.D. Student
Zhidong Zhou, Ph.D. Candidate

Department of Civil & Environmental Engineering
Washington State University
Pullman, WA 99164-2910

for

Pacific Northwest Transportation Consortium (PacTrans)
USDOT University Transportation Center for Federal Region 10
University of Washington
More Hall 112, Box 352700
Seattle, WA 98195-2700

In cooperation with US Department of Transportation-Research and Innovative Technology Administration (RITA)

Disclaimer

The contents of this report reflect the views of the authors, who are responsible for the facts and the accuracy of the information presented herein. This document is disseminated under the sponsorship of the U.S. Department of Transportation's University Transportation Centers Program, in the interest of information exchange. The Pacific Northwest Transportation Consortium, the U.S. Government and matching sponsor assume no liability for the contents or use thereof.

Technical Report Documentation Page

1. Report No.	2. Government Accession No.	3. Recipient's Catalog No.

4. Title and Subtitle	5. Report Date
Development of Surface-Mounted Smart Piezoelectric Modules for Condition Assessment of Bridges	
	6. Performing Organization Code

7. Author(s)	8. Performing Organization Report No.
Pizhong Qiao, Ayumi K. Manawadu and Zhidong Zhou	

9. Performing Organization Name and Address	10. Work Unit No. (TRAIS)
PacTrans Pacific Northwest Transportation Consortium University Transportation Center for Region 10 University of Washington More Hall 112 Seattle, WA 98195-2700	
	11. Contract or Grant No.
	DTRT13-G-UTC40

12. Sponsoring Organization Name and Address	13. Type of Report and Period Covered
United States of America Department of Transportation Research and Innovative Technology Administration	Research
	14. Sponsoring Agency Code

15. Supplementary Notes

Report uploaded at www.pacTrans.org

16. Abstract

In-situ, real-time structural health monitoring (SHM) of civil infrastructure via piezoelectric materials (PZT) is an emerging, sustainable method to ensure structural safety and integrity. In this study, a smart surface-mounted PZT patch system and an embedded PZT cement module system were developed to determine the wave modulus of elasticity (WMoE) of concrete through a combined experimental and numerical investigation. Concrete beams and a concrete panel were evaluated to identify the feasibility of utilizing the two smart PZT systems to determine the WMoE at different ages. The key parameter of the study was to determine the time of flight (ToF) of the first Rayleigh wave (R-wave) package from the surface-mounted PZT patch system or the first shear wave (S-wave) package from the embedded PZT cement module system of propagating waves. The experimentally measured WMoE from the two smart PZT systems were about 11 percent (maximum) higher than the SMoE of the concrete obtained from the compression test. The experimental results also indicated that the surface-mounted PZT patch system produced higher WMoE values than the embedded PZT cement module system, but within a range of 4 percent. The orientation of the embedded PZT cement modules affected the clarity and magnitude of the propagating wave. The established FE model for beams validated the results of the experimental evaluation. The measured WMoE also varied with the dimensions of the structures, and the WMoE values measured from a narrower, deeper structure were smaller than the ones from a wider, shallower structure. Overall, the surface-mounted PZT system proved to be as effective as or even better than the embedded PZT cement module system in determining the of WMoE concrete with a certain degree of confidence and in assessing concrete properties.

17. Key Words	18. Distribution Statement
	No restrictions.

19. Security Classification (of this report)	20. Security Classification (of this page)	21. No. of Pages	22. Price
Unclassified.	Unclassified.		NA

Form DOT F 1700.7 (8-72) **Reproduction of completed page authorized**

Table of Contents

List of Figures

List of Tables

List of Abbreviations

AE	Acoustic emission
AEA	Air entraining admixture
COV	Coefficient of variation
DOF	Degree of freedom
FE	Finite element
GGBFS	Ground granulated blast-furnace slag
HRWRA	High-range water reducing admixture
NDT	Nondestructive testing
P-wave	Longitudinal wave
PZT	Lead zirconate titanate, a piezoelectric ceramic material
R-wave	Rayleigh wave
SA	Smart aggregate
SF	Silica fume
SHM	Structural health monitoring
SMoE	Static modulus of elasticity
S-wave	Shear wave
ToF	Time of flight
WMoE	Wave modulus of elasticity
WSDOT	Washington State Department of Transportation

Acknowledgments

This project is funded by a grant from the U.S. Department of Transportation through the Pacific Northwest Transportation Consortium (PacTrans).

Executive Summary

To determine the most suitable techniques and timing for bridge maintenance, it is necessary to assess the condition of concrete bridges and evaluate the type and severity of damage. The information is helpful to identify concrete bridges in critical condition and to allocate funds more effectively. However, most widely used methods for assessing the condition of bridges, such as visual inspection and laboratory testing of core samples, are difficult to implement and expensive, and they do not provide the whole picture about the condition of a structure. The existing non-destructive testing methods available for inspecting concrete structures all suffer from limitations in accuracy, cost, maneuverability, in situ capability, and implementation. Also, most of the laboratory-based investigation methods lack of practicality and applicability to in-field structural health monitoring. Hence, most of these methods are not used in practical applications. Therefore, it is necessary to develop cost effective, convenient methods that are capable of being applied in situ and to real-time structural health monitoring, and that will facilitate the collection of information on the condition and premature failure of highway bridge structures during their service life. Such information can be amalgamated to a database to support effective decision making on bridge repair and maintenance routines that will avoid property damage and human injury.

The goal of the present study was to develop viable tools that utilize ultrasonic smart piezoelectric material (lead zirconate titanate, PZT) to assess the material property (primarily in terms of the wave modulus of elasticity, WMoE) of concrete, thereby identifying the condition of concrete bridges. The primary objective of the proposed study was to determine the effectiveness of utilizing a surface-mounted PZT patch system and an embedded PZT cement module system to

determine the WMoE of concrete. As most of the present literature has focused on the material property assessment of concrete structures using the embedded PZT cement module system, the proposed study focused on identifying the feasibility of using a surface-mounted PZT patch system in the material property assessment of concrete structures. The embedded PZT cement module system is less practical because of difficulties in accurately positioning the PZT cement module during construction and in placing the PZT cement modules in existing structures (in terms of destructively drilling concrete to insert the cement modules). Nevertheless, the embedded PZT cement module system was also used for comparison purposes in this study.

A combined experimental and numerical investigation was conducted on concrete beams and a concrete panel using both the smart surface-mounted PZT patch and the embedded PZT cement module systems. The ideal orientation of the PZT cement modules, distance of the PZT pairs, and concrete dimension effects were investigated. With the embedded PZT cement module system, the arrival time of the first shear wave (S-wave) package of the response signal was compared with the input signal to obtain the time of flight (ToF) of the propagating wave. Similarly, the first Rayleigh wave (R-wave) package from the surface-mounted PZT patch system was utilized to determine the ToF. A numerical finite element (FE) analysis was performed to investigate the concepts of piezoelectric effect and wave propagation and to verify the accuracy of the experimental results.

We found that the surface-mounted PZT patch system generally produced a higher estimation of the WMoE than the embedded PZT cement module system. The orientation of the embedded PZT cement module had an influence on the clarity and magnitude of the response signals. However, the effects on the estimated ToF and WMoE due to variations in the orientation of the embedded PZT cement modules were insignificant. The numerical FE predictions of the

WMoE with the input of the static modulus of elasticity (SMoE) value from the compression test were consistent with the experimentally determined results for the two systems. The experimental investigation based on the surface-mounted PZT patch system further indicated that the estimated WMoE had a dependence on the dimensions of the structure. The WMoE values measured from a narrower, deeper structure were smaller than the ones from a wider, shallower structure. However, the surface-mounted PZT patch system produced satisfactory results for a narrower structure with a large depth, despite the boundary reflections.

In summary, the surface-mounted PZT system is as effective as or even better than the embedded PZT cement module system in determining the WMoE of concrete with a certain degree of confidence and assessment of concrete properties. The surface-mounted PZT patch system has more advantages in terms of monitoring and assessing existing concrete structures than the embedded PZT cement module system because the PZT patches can be nondestructively surface-mounted to concrete structures. Therefore, it is a promising alternative nondestructive technique for determining the WMoE of concrete structures. However, the surface-mounted PZT patch system represents the measurement of WMoE within only one wave length of depth, and it may be not truly reflect the WMoE of all the interior of the concrete.

Further investigations are also recommended, such as the ability of the surface-mounted PZT patch system to detect the presence of cracks, the effects of freeze/thaw attacks, and corrosion of reinforcement in the concrete. The capabilities of the two smart PZT systems considered in this study should be expanded to large-scale civil infrastructure, and implementation tests should be carried out in real, large-scale structures to assess the feasibility of using such systems in practical applications when the conditions are not ideal.

Chapter 1 Introduction

Timely maintenance of highway bridges is necessary to ensure the safety of travelers. Damage types (e.g., cracks, damage due to material property degradation, impact damages, fatigue, etc.) and severities determine the rehabilitation and maintenance techniques required. Also, such information is helpful to identify which bridges need immediate attention and to estimate the cost of maintenance. Furthermore, a database containing information on the condition of bridges, such as damage and material property degradation, could be used to support future research.

Popular condition assessment techniques, such as visual inspection and laboratory testing of core samples from existing concrete structures, are expensive and tedious to conduct. In addition, the results do not reveal situation of whole structures. Furthermore, large size, complex geometries, and accessibility issues limit the application of such methods. Non-destructive testing (NDT) methods, such as impact echo, impulse response, radiography, acoustic emission, thermal field, etc., are also used to assess the condition of concrete structures (Rehman et al., 2016). However, the limited accuracy, excessive costs, maneuverability issues, and limited in-situ application of these methods have confined them mostly to research and laboratories. Therefore, there is a pressing need to develop an effective, continuous, in-situ health monitoring system to assess the condition of highway bridges.

Structural health monitoring (SHM) of civil infrastructure via NDT that incorporates piezoelectric sensors is an emerging, sustainable method to ensure structural safety and integrity. Inclusion of PZT (lead zirconate titanate) in SHM has been identified as an effective technique for the real-time assessment of the physical and mechanical properties of complex civil engineering materials, such as concrete. PZT is a type of piezoelectric ceramic that is widely used as a sensor/actuator in civil engineering and aerospace applications because of its inherent advantages,

such as light weight, sensitivity, repeatability, small size, low cost, wide bandwidth, etc. PZT-generated acoustic waves, in combination with post-processing techniques, are used to identify material property variations over the lifetime of structures and to detect and characterize associated degradation and damage. However, one of the main complications of using PZT is that it produces waves in all directions under the influence of an applied electric field. Therefore, identifying the correct wave package for analysis is of great importance. Moreover, the influence of many boundary reflective waves and the hexagonal symmetry of PZT with respect to piezoelectric and elastic properties make the task more difficult.

In this study, a combined experimental and numerical approach was used to develop the NDT technique of using a surface-mounted PZT patch system to assess the material property of concrete. An experimental investigation was first performed on concrete beams to compare the feasibility of utilizing the surface-mounted PZT patch system with that of an embedded PZT cement module system in determining the wave modulus of elasticity (WMoE) of concrete at different ages. The PZT cement patches are produced as a cement casing surrounding PZT discs, to ensure easy installation, durability, and robustness of the embedded PZT patches in concrete.

Numerical modeling of both the surface-mounted and embedded PZT in concrete was performed with commercially available finite element (FE) software to verify the concepts used in the experimental investigation and to better understand the complex phenomena of mechanical wave generation and propagation by the PZT actuators and sensors. The first shear wave (S-wave) package produced by the embedded PZT cement modules was utilized to calculate the time of flight (ToF) of propagating waves, which was used to determine the WMoE of concrete at given periods of cement hydration. The orientation of the embedded PZT cement modules was also varied to better understand the effects of PZT placement in concrete on wave generation and

propagation. Furthermore, the validity of the surface-mounted PZT patch system for assessing the material property of concrete was investigated at predetermined times. The ToF of the first Rayleigh wave (R-wave) package was used for calculations related to the surface-mounted PZT patch system. The WMoE from the experimental investigation was compared with the results from the numerical FE analysis. The static modulus of elasticity (SMoE) of concrete was obtained through a compression test. The SMoE values were established as the reference for the study to form the basis of comparison between the experimental and numerical WMoE of concrete. Then the results from both the surface-mounted PZT patch and the embedded PZT cement module systems were compared with each other to understand the deviations in the measured WMoE. A recommendation was made for their application to in situ material assessments.

The applicability of PZT actuator-sensor arrays to bulk concrete was also investigated by using a concrete panel. For comparison purposes, the WMoE estimated with the embedded PZT cement module system was also found for the same bulk concrete structure. To test the applicability of the concept on bulk concrete, a concrete panel was cast with embedded PZT cement modules and surface-mounted PZT patches. The intention was to determine how effective the surface-mounted PZT patch system is when the structure consists of concrete with larger depths. We also intended to observe how the PZT sensor array concept would work on bulk concrete. Actuator-sensor arrays are relatively popular in determining the properties of isotropic metals and composite plates, whose thicknesses are very thin. However, studies on the application of this concept to bulk concrete are very limited because of the most obvious complications in the propagation of waves and the inhomogeneous nature of concrete. Several types of waves propagate in bulk concrete structures, where the R-wave penetrates only one wavelength depth. Therefore,

the surface-mounted PZT patch system must be used with care for detecting the internal changes of structural materials.

Finally, the effects of varying distances among PZT actuator-sensor pairs in determining the WMoE were also investigated in this study.

Chapter 2 Literature Review

This chapter focuses on the fundamentals of piezoelectric materials, ultrasonic wave propagation in solids, and past studies conducted on the application of piezoelectric sensors in monitoring the health of concrete structures.

2.1 Piezoelectric Materials

2.1.1 Piezoelectric Effects

Smart materials can change their properties in response to variations in the environment, such as temperature, electricity, light, or pressure. Piezoelectric materials are a sub-class of smart materials that can develop a potential across their boundaries when subjected to pressure or mechanical stress. This phenomenon is known as the direct piezoelectric effect, and it was first observed by the Curie brothers (1880). The direct piezoelectric effect is an attractive property for sensor applications, that is, to generate an electric response when subjected to an external stress field. This response signal can then be observed by digital means. This property is linear and reversible. Lipmann (1881) found the existence of a converse piezoelectric effect through thermodynamics principles, which means the property of the piezoelectric material generates a mechanical stress or strain wave when it is placed in an electric field. This property makes it a suitable candidate for actuator applications. This linear electromechanical interaction between the material's electrical and mechanical energy has made piezoelectric material an attractive alternative for many sensor/actuator systems in medical, military, non-destructive testing, communications, energy harvesting, and automotive applications. (Bhalla et al., 2017; Jordan and Ounaies, 2011).

The secret behind the piezoelectric effect is the displacement of ionic charges in crystals with no center of symmetry (Jordan and Ounaies, 2011). Because of the lack of center of symmetry

of such crystals, the positive and negative charges tend to displace with respect to each other when an external stress is applied. This action creates electric dipoles that lead to an electric field. However, the orientation of such dipoles is highly random, and the net effect is insignificant. A process known as "polling" is carried out to align the electric dipoles in the desired direction.

2.1.2 Available Piezoelectric Materials

Piezoelectric properties can be found in many natural and manmade materials. Some materials that possess piezoelectric properties include natural materials such as quartz, Rochelle salt, topaz, berlinite and sucrose; biological materials such as dry bones, tendons, and silk; synthetic ceramics such as lead zirconate titanate (PZT), barium titanate, and potassium niobate; and polymers, such as polyvinylidene fluoride (PVDF) (Jordan and Ounaies, 2011). The most commercially utilized piezoelectric material is PZT, which exhibits very high piezoelectric, dielectric, and ferroelectric properties. This material is based on a perovskite structure, which does not show any polarization beyond the Curie temperature (Jordan and Ounaies, 2011). Piezoelectric transducers made of PZT are popular in ultrasonic sensing applications because of their high sensitivity, applicability to active sensing, low cost, quick response, and availability in different shapes and small sizes (Song et al., 2008). These make PZT sensors a suitable candidate for the in-situ health monitoring of structures.

2.1.3 Constitutive Relationships of Piezoelectric Material

It is necessary to understand that piezoelectric materials behave by using constitutive relationships when a mechanical stress wave or an electrical field is present. The constitutive relationship of piezoelectric materials are of two matrix forms, as indicated in equations (2.1) and (2.2) (Jordan and Ounaies, 2011; Shirohi and Chopra, 2000). As shown in equation (2.1), the mechanical strain (S) is related to the electric field (E) and the stress field (T) by the piezoelectric constant (d) and the compliance matrix (s). In equation (2.2), the electric displacement (D) is

related to E and T by the dielectric constant (ε) and d. Here, s is measured at the constant electric field, and ε is measured at the constant stress field.

$$\{S\} = [d^t]\{E\} + [s^E]\{T\} \quad (2.1)$$

$$\{D\} = [\varepsilon^t]\{E\} + [d]\{T\} \quad (2.2)$$

where the superscript t stands for the transposition of a matrix. More complex equations with thermal effects have also been developed (Cady, 1946; Giurgiutiu, 2008; Ikeda, 1990). The interaction between the electrical, mechanical, and thermal effects are complicated and will not be discussed here.

Particularly in equation (2.1), in addition to the general constitutive relationship of stress-strain from applied forces, there is an additional term that represents the contribution to the mechanical strain from the applied electric field. This equation elaborates the converse piezoelectric effect. The additional contribution from the mechanical stress to the electric displacement is incorporated in equation (2.2), and it elaborates the direct piezoelectric effect. Analysis could be done on the basis of either of the two approaches. Another crucial point to note is that piezoelectric material is transversely isotropic in the direction perpendicular to the polling axis. The usual practice of defining the axis system is shown in figure 2.1. For a PZT sensor polled in direction 3, the matrix given in equation (2.3) indicates the compliance constant, in equation (2.4) the piezoelectric constant, and in equation (2.5) the dielectric constant.

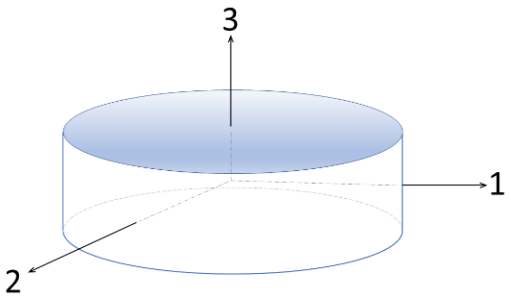

Figure 2.1 Axis system for the PZT patch

$$[s]=\begin{bmatrix} s_{11} & s_{12} & s_{13} & 0 & 0 & 0 \\ s_{12} & s_{11} & s_{13} & 0 & 0 & 0 \\ s_{13} & s_{13} & s_{33} & 0 & 0 & 0 \\ 0 & 0 & 0 & s_{44} & 0 & 0 \\ 0 & 0 & 0 & 0 & s_{44} & 0 \\ 0 & 0 & 0 & 0 & 0 & 2(s_{11}-s_{12}) \end{bmatrix} \tag{2.3}$$

$$[d]=\begin{bmatrix} 0 & 0 & 0 & 0 & d_{15} & 0 \\ 0 & 0 & 0 & d_{15} & 0 & 0 \\ d_{31} & d_{31} & d_{33} & 0 & 0 & 0 \end{bmatrix} \tag{2.4}$$

$$[\varepsilon]=\begin{bmatrix} \varepsilon_1 & 0 & 0 \\ 0 & \varepsilon_1 & 0 \\ 0 & 0 & \varepsilon_3 \end{bmatrix} \tag{2.5}$$

2.2 Ultrasonic Waves

Ultrasonic wave-based testing utilizes high frequency sound waves in damage detection and material property assessment processes. When a PZT patch (actuator) is placed in an electric field, it transforms electric energy to mechanical energy, producing a mechanical stress wave. This ultrasonic wave is captured by a distanced PZT sensor, which converts mechanical energy back to electrical energy and produces an electrical signal output. This response signal can then be captured and analyzed by digital means.

In solids, sound can propagate in diverse ways, depending on the particle oscillation and the thickness of the material. Waves can be categorized mainly into two sections, as bulk waves (longitudinal waves and shear waves) and surface waves (Rayleigh waves). Longitudinal wave (P-wave) oscillations occur in the direction of wave propagation, and the energy travels by compression and expansion. In contrast, the shear waves (S-wave) or transverse waves oscillate the particle perpendicular to the direction of propagation. These two types of bulk waves can be observed in the case of embedded PZT based sensors. P-waves usually have a higher velocity and a lower amplitude, while S-waves usually have a higher amplitude with a lower velocity. Rayleigh waves (R-wave) are generated near the surface of a relatively thick material, effective up to one wavelength depth. The particle vibration of R-waves follows an elliptical orbit motion in which the major axis of the ellipse is normal to the surface. The width of the elliptical motion is inversely proportional to the depth of the particle from the surface. R-waves are sensitive to surface defects and useful to analyse structures with complex geometries. This type of wave has a higher amplitude and a lower velocity than bulk waves.

2.3 Piezoelectric Actuators and Sensors in Monitoring the Health of Concrete Structures

In the presence of an electric field, piezoelectric material as an actuator produces mechanical stress waves. These ultrasonic waves travel through the structure and can be detected by another piezoelectric sensor placed at the far end. Depending on the changes in certain parameters of the excitation signal and the response signal, many structural properties can be determined. Piezoelectric actuators and sensors usually can be embedded in protecting cement gel in modules or smart aggregate (SA) or surface-mounted in patches. Many investigations have been carried out to utilize piezoelectric actuators and sensors for monitoring the health of concrete structures (Gu et al., 2006; Hu et al., 2013; Li et al., 2016; Liu et al., 2013; Moslehy et al., 2010; Qiao et al., 2011; Tseng and Wang, 2014; Yan et al., 2009).

Gu et al. (2006) studied the ability of embedded piezoelectric sensor/actuator systems to monitor the strength gain in early age concrete by using high frequency vibration waves. PZT patches in the form of SA, which were small, precast concrete cylinders with embedded PZT patches and like aggregate in shape, were utilized to conduct the experimental testing. The investigation indicated that the amplitude of the harmonic response decreased rapidly in the first seven days after casting, followed by a gradual decrease as hydration proceeded.

Hu et al. (2013) studied the feasibility of using SA to detect both artificial and real cracks in concrete through P-waves. The SA was found to be a suitable candidate to detect not only artificial cracks but also the cracks initiated in flexure, including notches, holes, inclusions and cracks. They also observed that the response signal became weaker in the presence of inclusions or increased notch size and hole diameter.

Qiao et al. (2011) utilized SA to determine material degradation due to freeze-thaw attacks and to detect artificial damages (saw-cuts) in both recycled aggregate concrete and natural aggregate concrete. The time of flight (ToF, the arrival time difference between the peaks of the excitation and response signals) of the first shear wave package was the key parameter in the experimental program, which was related to the WMoE of the constituent material. The WMoE decreased as the number of freeze-thaw cycles increased, and the measured WMoE showed good agreement with the ones from dynamic modulus testing, indicating the capability of SA to determine the WMoE of concrete. Despite its broad range of uses, it is difficult to embed SA precisely in a desired location or orientation. In addition, if SA is to be used with an existing structure, it has to be inserted by drilling, which comes with additional costs and efforts.

Many researchers have also mounted PZTs on the surfaces of structures, instead of embedding them in the form of SA. Song et al. (2008) numerically and experimentally studied the

behavior of the response signals from te surface-mounted PZT patches over varying distances. They determined that the response signals from surface-mounted PZT patches did not attenuate over a longer distance.

Sun et al. (2008) studied the applicability of surface-mounted PZT patches to detecting the dynamic elastic modulus and dynamic Poisson's ratio of concrete beams in comparison to observations from embedded SA utilizing P-waves. Lim et al. (2016) utilized these two parameters to effectively predict the strength gain of concrete during the curing period. Li et al. (2016) compared surface-mounted acoustic emission (AE) sensors with embedded SA to detect natural cracks in concrete. The main advantage of such surface-mounted PZT patches is that they can be effectively attached to the surface of existing structures at any time after construction and on a desired location.

Chapter 3 Materials and Methods

In this chapter, the materials used to prepare concrete samples are presented along with related experimental and numerical methods to study wave propagation in concrete. In addition, the determination of the WMoE of concrete with the surface-mounted PZT patch and embedded PZT cement module systems is described in detail.

3.1 Materials and Mix Design

In this study, the cement used was Portland cement (Type I-II), along with other cementitious materials (i.e., silica fume (SF) and ground granulated blast-furnace slag (GGBFS)). Coarse aggregates and fine aggregates (sand) were provided by Pre-mix, Inc., a local concrete company in Pullman, Washington. The gradation of coarse and fine aggregates, along with the corresponding specific gravity and water absorption are presented in table 3.1. Coarse and fine aggregates for concrete mix meet the requirements of AASHTO #8 and Washington State Department of Transportation (WSDOT) Class 2 Sand. Air entraining admixture (AEA) and high-range water reducing admixture (HRWRA), produced by BASF Construction Chemicals, LLC, were also used in the concrete mix. Grace Construction Products provided 1000 air-entraining admixture to produce proper air content in the mixture. Glenium 3030 NS, a polycarboxylate-based HRWRA, was used to achieve the desired workability. The amounts of AEA and HRWRA for concrete were determined on the basis of the measurements of air content and slump of the fresh concrete. The details of the mix design, following WSDOT guidelines, are summarized in table 3.2. The properties of the piezoelectric PZT patch from Steiner & Martins, Inc. (SMD10T04R111WL), with a resonant frequency of 5 MHz, are indicated in table 3.3.

Table 3.1 Fine and coarse aggregate gradations (sieve analysis)

Sieves #	Coarse aggregate, Cumulative % Passing	Fine aggregate, Cumulative % Passing
1/2	100	--
3/8"	99.1	100.0
1/4"	37.3	99.5
#4	6.9	85.7
#8	3.2	58.5
#16	1.8	35.6
#30	1.2	16.0
#50	0.9	4.8
#100	0.8	2.1
#200	--	--
Specific Gravity	2.69	2.64
Absorption Capacity, %	1.21	1.89

Table 3.2 WSDOT mix design

Constituents	Cement (kg/m^3)	Silica Fume (kg/m^3)	GGBFS (kg/m^3)	Coarse (kg/m^3)	Sand (kg/m^3)	w/cm	Water (kg/m^3)
Amount	240	30	24	1258	469	0.34	158

Table 3.3 Material properties of the PZT patch

Elastic constants (N/m^2)	Piezoelectric constants (m/V)	Dielectric constants (C/Vm)
$c_{11} = 8.6 \times 10^{10}$	$d_{31} = -140 \times 10^{-12}$	$D_{11}=1.395 \times 10^{-8}$
$c_{12} = 4.8 \times 10^{10}$	$d_{33} = -320 \times 10^{-12}$	$D_{33} = 1.24 \times 10^{-8}$
$c_{13} = 4.9 \times 10^{10}$	$d_{15} = 500 \times 10^{-12}$	
$c_{33} = 7.3 \times 10^{10}$		
$c_{44} = 3.0 \times 10^{10}$		
$c_{66} = 1.9 \times 10^{10}$		

3.2 Preparation of Samples

3.2.1 PZT Cement Modules

The PZT cement modules were prepared according to the guidelines given by Song et al. (2008) in the preparation of smart aggregates. Cement modules normally encase the brittle PZT patches and protect them from potential external damage during and after construction of concrete structures. A PZT patch with dimensions of 10 mm × 10 mm × 0.4 mm and a cement module with dimensions of 19 mm (diameter) × 19 mm (thickness) were used in this study. All surfaces of each PZT patch were first coated with a thin layer of epoxy resin to form a waterproofing film. The cement modules were prepared with concrete mortar (cement: sand: water = 1: 1.5: 0.48) in two layers in a plastic mold. The epoxy-coated PZT patch was positioned between these two mortar layers perpendicular to the cylindrical axis. Finally, a copper ribbon was wound around the PZT cement module for better electric conductivity. The PZT cement modules were initially cured in water for 28 days before being embedded in concrete beams and panels. The steps of preparing the PZT cement modules are illustrated in figure 3.1.

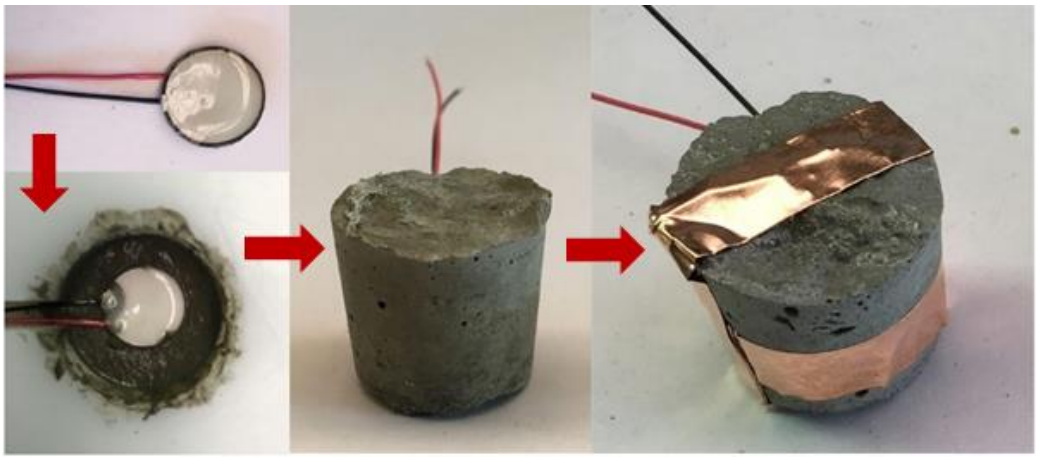

Figure 3.1 Preparation of the smart PZT cement modules

3.2.2 Concrete Beam Samples

Three concrete beams with dimensions of 75 mm × 100 mm × 400 mm were cast with embedded PZT cement modules in three different orientations (θ = 0º, 45º, and 90º), as shown in figure 3.2. For reference purposes, the beams with θ = 0º, 45º and 90º were named as B#1, B#2 and B#3, respectively. The surface-mounted PZT actuator and sensor patches were referred to as SM1 and SM2, respectively, while the respective embedded PZT cement modules in the beams were referred to as EM1 and EM2. Concrete was poured in two layers into the greased steel molds. After the initial layer had been poured up to a 50-mm depth, the PZT cement modules were held on desired locations. Then the next layer of concrete was poured on top. The distance between the two PZT cement modules (EM1 or EM2) was fixed at approximately 350 mm. Concurrently, to investigate the effectiveness of the use of surface-mounted PZT sensor/actuator systems, two circular PZT patches (SM1 and SM2) were mounted with epoxy resin onto the top surface of each concrete beam. The distance between the two PZT patches was also maintained at 350 mm, as above. The PZTs on the surface were attached to the beams the day following casting of the beams and were left untouched for 24 hours to cure the epoxy. All beams were air cured in the laboratory for the first 28 days after casting.

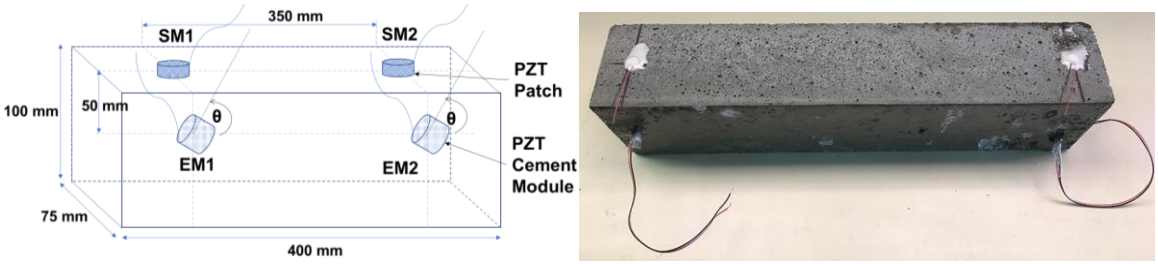

Figure 3.2 Concrete beam with surface-mounted PZT patches and embedded PZT cement modules

3.2.3 Bulk Concrete Panel

In parallel, a concrete panel with dimensions of 600 × 600 × 100 mm was cast with an array of embedded PZT cement modules, as shown in figures 3.3 and 3.4. The concrete was placed in two layers. After the initial layer had been poured up to a 50-mm depth, PZT cement modules were placed in desired locations with two wooden sticks as guides. Then the next layer was poured on top of it. The set-up used to ensure correct positioning of the SA, as shown in figure 3.5. Because concrete without inclusion of large size aggregate was utilized, no external vibrations were used throughout the casting process. As previously mentioned, the precise placement of PZT cement modules is difficult. The panel was demolded after 24 hours. Simultaneously, to investigate the effectiveness of the use of the surface-mounted PZT patch system, the circular PZT patches were mounted with epoxy resin on the top surface and the side surface of the concrete panel. For reference purposes in this testing set-up, the PZT cement modules and the surface-mounted PZT patches were labelled as shown in figure 3.6. The embedded PZT cement modules were labelled with the suffix E, while the surface-mounted PZT patches on the top surface (shown in red in figure 3.3) were labelled with the suffix S. The side surface of the panel was also utilized to observe the capability of the surface-mounted PZT patch system to determine the WMoE of concrete at

larger depths. These PZT patches on the side surface were labelled with the suffix SS, as shown in orange in figure 3.3.

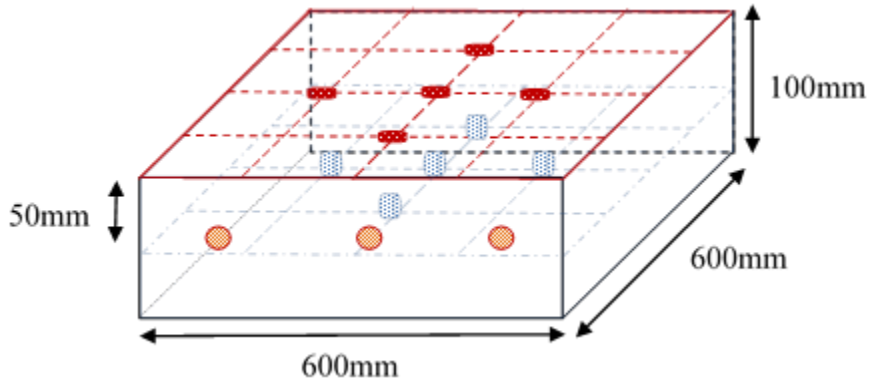

Figure 3.3 Concrete panel for material property assessment using the surface-mounted PZT patches and embedded PZT cement modules

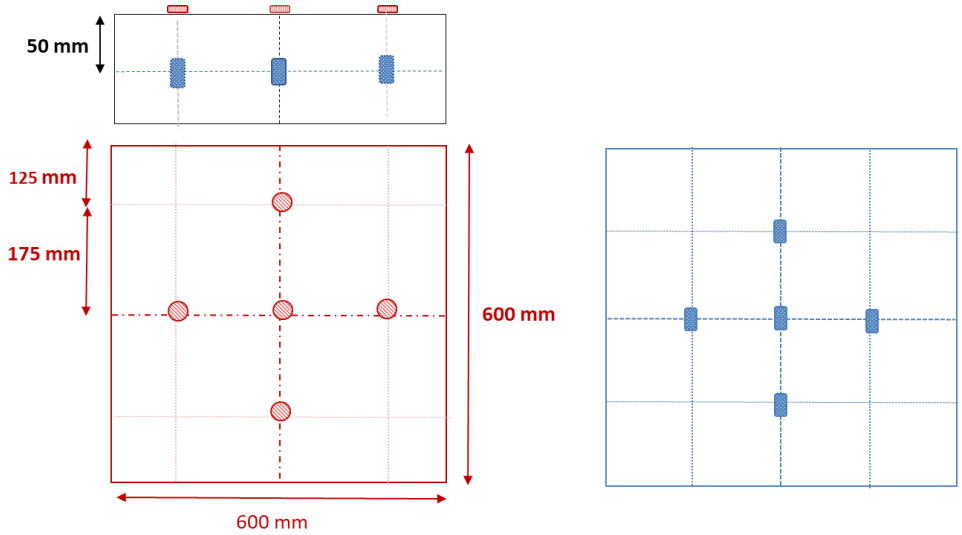

Figure 3.4 Elevations of concrete panel installed with the surface-mounted PZT patches and embedded PZT cement modules

Figure 3.5 Casting of bulk concrete panel and placement of embedded PZT cement modules

Figure 3.6 Labelled PZT patches on and embedded PZT cement modules in the concrete panel: embedded PZT cement modules (E-A to E-D and E-O), surface-mounted PZTs (S-A to S-D and S-O), and side surface-mounted (SS-A, SS-C and SS-O)

3.3 Basic Mechanical Property Tests

A series of tests was conducted to evaluate the mechanical properties of the concrete in its fresh and hardened states. Slump and unit weight were measured to evaluate the related properties of the fresh mix. The related mechanical properties of the hardened concrete were tested at different ages, including the compressive strength, static modulus of elasticity, etc. This information about concrete was useful as input for further FE analysis. The procedures for each test in the three categories above are briefly discussed in the following sections, and the tests considered in this study are summarized in table 3.4 along with their corresponding ASTM standard test method designations. For all tests, at least three replicates were tested.

Table 3.4 Experimental testing program

Properties	Test Methods	Condition
Fresh Properties of Shotcrete		
Slump	ASTM C143	Fresh
Unit Weight	ASTM C138	Fresh
Hardened Properties of Shotcrete		
Compressive Strength	ASTM C39	150 × 300 mm cylinder@ 7, 14, and 28 days
Static Modulus of Elasticity (SMoE)	ASTM C469	150 × 300 mm cylinder@ 7, 14, and 28 days

The slump test (figure 3.7) was performed following the procedures of ASTM C143 (2015), "Standard Test Method for Slump of Hydraulic Cement Concrete." In the meantime, the unit weight of fresh shotcrete was determined by following the procedures of ASTM C138 (2016), "Standard Test Method for Density (Unit Weight), Yield, and Air Content (Gravimetric) of Concrete." The compressive strength test was conducted on 150-mm × 300-mm cylinders

following the procedures of ASTM C39 (2016), “Standard Test Method for Compressive Strength of Cylindrical Concrete Specimens” (figure 3.8). The compressive test was conducted under a specific stress rate, 0.25 ± 0.05 MPa/s. Therefore, the required loading rate was calculated in correspondence with the size of the specimen, i.e., 265 ± 53 kN/min. The static modulus of elasticity (SMoE) of concrete was obtained by following the procedures of ASTM C469 (2014), “Standard Test Method for Static Modulus of Elasticity and Poisson’s Ratio of Concrete in Compression” (figure 3.9). The load was applied in correspondence with a specific stress rate, 0.25 ± 0.05 MPa/s, until it reached 40 percent of the average ultimate load of the 150-mm x 300-mm cylindrical specimens.

Figure 3.7 Slump test

Figure 3.8 Compressive strength test

Figure 3.9 Modulus of elasticity test

3.4 Experimental Procedures of the Wave Analysis

3.3.1 Experimental Set-Up and Procedures

The experimental set-up for the wave propagation test consisted of an arbitrary waveform generator (Agilent 33120A), a power amplifier, a Butterworth filter (model 3382), an oscilloscope and a computer, as shown in figure 3.10. The input signal produced from the arbitrary waveform generator was amplified and sent to the actuator of the PZT cement module system and surface-mounted PZT patch system, one at a time. The actuator then transformed the signal to a mechanical stress wave, which traveled through the concrete structure. This ultrasonic wave was detected by the surface-mounted PZT patch or embedded PZT cement module working as the sensor, and it used the direct piezoelectric effect to transform this stress wave back to an electrical response. The oscilloscope captured the input signal as well as the output signal and the digitized waves were processed with a computer. After some trial experiments had been conducted with varying wave frequencies from 70 kHz to 180 kHz, a wave frequency of 100 kHz was chosen to obtain relatively

clearer waveforms in this study. From the entire range of frequencies, the frequencies from 90-110 kHz were observed to give the strongest sensor response for the majority of the cases investigated. A 3.5 cycles Hanning windowed sinusoidal wave with a frequency of 100 kHz was used as the excitation signal, as defined by equation (3.1). The graphical representation of the wave is show in figure 3.11. The experimental investigation captured 1,000 sampling points at an interval of 0.5 μs. The band range Butterworth filter significantly reduced both the upper bound and lower bound noise, eliminating the need to use complex mathematical processing to improve the clarity of the signals.

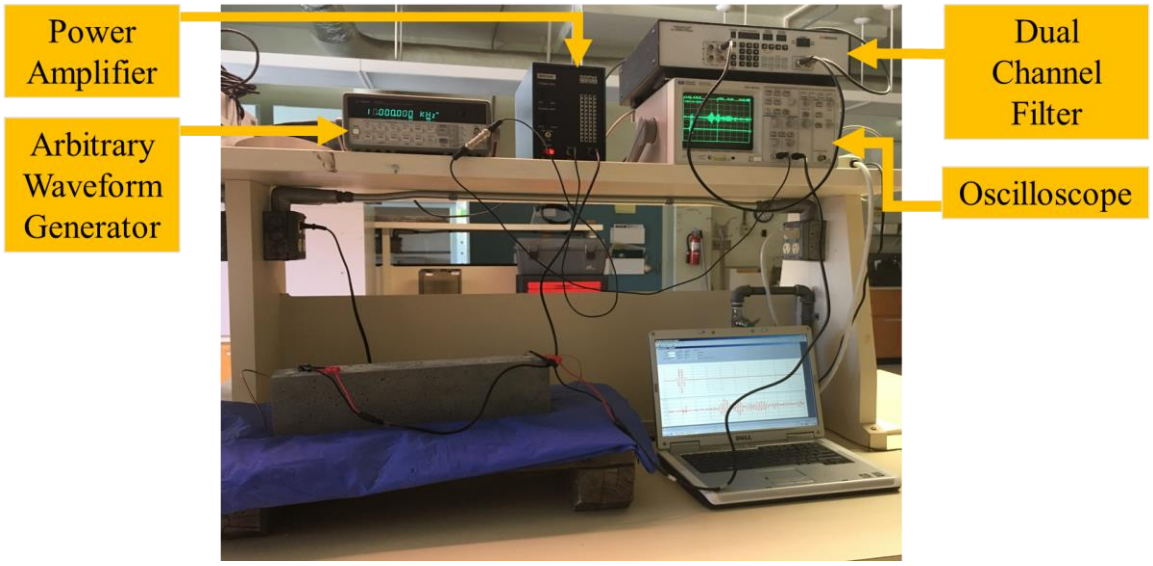

Figure 3.10 Experimental set-up for the determination of WMoE of concrete

$$S(t) = 0.5\left\{1 - \cos\left(2\pi t \times 100 \times \frac{10^3}{3.5}\right)\right\} \times \sin(2\pi t \times 100 \times 10^3) \quad 0 \leq t \tag{3.1}$$

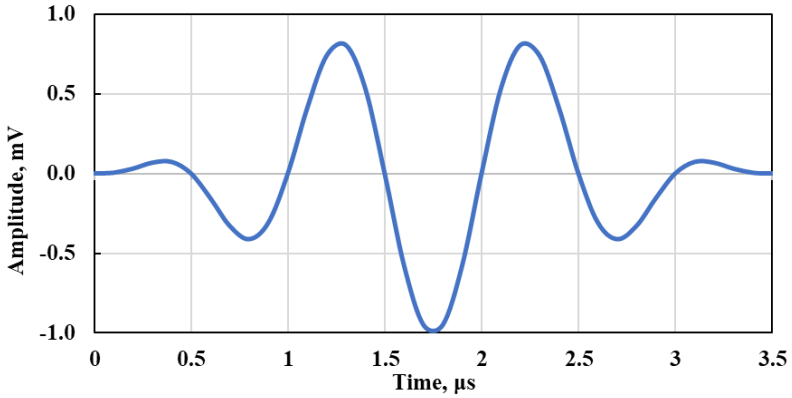

Figure 3.11 100 kHz 3.5 cycles Hanning windowed sinusoidal wave as the input signal

3.2.2 Experimental Investigation of Concrete Beams

The amplified input signal produced by the arbitrary waveform generator was sent to SM1 (the surface-mounted actuator), as indicated in figure 3.2. Once the SM1 transformed the electrical signal to mechanical stress waves and it traveled through the beam, the response signal was obtained from SM2 (the surface-mounted sensor) in electrical form. Similar transformations happened in between EM1 (the embedded PZT module-actuator) and EM2 (the embedded PZT module-sensor), respectively. The excitation and response signals of the three beams with the embedded PZT cement modules were recorded at 3, 7, 10, 14, 21, and 28 days after casting of the concrete beams. Data from the surface-mounted PZT patches were obtained at 4, 7, 10, 14, 21, and 28 days.

3.2.3 Experimental Investigation of Concrete Panel

A procedure similar to that for the concrete beam samples was followed for the concrete panel. The purpose of instrumenting the concrete panel with both PZT systems was to evaluate their applicability in real concrete structures. Each surface-mounted PZT patch (S-labelled in figure 3.6) was actuated one at a time, and the response signal was obtained from each one of the remaining PZT patches on the same surface. This was done separately from the surface-mounted

PZT patches on the side surface (SS-labelled), as well as with the embedded PZT cement modules (E-labelled) (also see figure 3.6). Input and output signals were obtained on days 3, 7, 10, 14, 21, and 28 after casting.

3.5 Numerical Analysis

This section describes the wave generation, propagation, and reception studied with a 3D FE model that was constructed with commercially available FE software ABAQUS 6.10.1. To numerically verify and compare results from the experimental WMoE, two major components (including the PZT cement modules / PZT patches, and the concrete beam) were constructed in the FE model. A separate stand-alone analysis was performed for the PZT cement module to verify its functionality.

3.5.1 FE Model of PZT Cement Module System

The PZT cement module was modelled as a concrete cylinder encasing a PZT patch. Eight-node piezoelectric elements and 20-node linear brick elements under a full integration scheme were used to model the PZT patch and concrete, respectively. However, a selective refined mesh with a reduced integration scheme was also suitable for computational efficiency. The material properties of the PZT shown in table 3.5 and other relevant information of the concrete shown in table 3.4 were used to construct the FE model. Because PZT is not an isotropic material, the local material orientation needed to be specified. Material property matrices were reformulated according to standard notation in ABAQUS, where double subscripts of the second order tensors 11, 22, 33, 12, 13, and 23 were replaced by the corresponding single subscript vector components 1, 2, 3, 4, 5, and 6, respectively.

Table 3.5 Geometric and physical parameters of material relevant to the FE model

Material	Modulus of Elasticity (GPa)	Poisson's Ratio	Density (kg/m^3)	Physical Dimensions (m)		
				Length	Width	Thickness
Concrete	24.1	0.2	2,400	0.40	0.075	0.10
Modified PZT-4	-	-	7,800	0.01	0.01	0.004

The number of numerical reflections in an FE model depends on the number of elements per wavelength of the propagating wave and the polynomial order of the element shape functions (Drozdz, 2008). Therefore, at least seven elements per wavelength should be used to obtain satisfactory results. Accordingly, the linear elements with 2.5-mm mesh seeds were selected to comply with accuracy requirements, without compromising much on efficiency. Surface-based tie constraints were used to tie the PZT (master surface) with the concrete casing (slave surface), to ensure the contacting surface of structure was compatible with the response from the PZT patch. The slave surface was finely meshed in comparison to the master surface, to ensure efficient analysis of the model. In ABAQUS terminology, the electric potential was defined as degree of freedom 9 (DoF 9). Coupling equations were used to couple the electric potential degree of freedom (DoF 9) of the top and bottom surfaces of the PZT patch to the master nodes assigned to each surface. These master nodes were used to obtain the field and history output data from the analysis. The electric potential (EPOT) was picked from both the field and history output data, along with the displacement fields. For this stage of the analysis, the bottom surface of the PZT cement module was fixed. Then a static general step was initiated with a linear input signal to observe the variation of the displacement field with a linear electric potential. The electric field

was applied to the top surface of the PZT, while the electric potential of the bottom surface was set to zero.

3.5.2 Wave Propagation Using the FE Model

Three separate beams were numerically simulated for different orientations (θ) of PZT patches to study wave propagation in plain concrete using the embedded PZT cement module system. PZT cement modules with three different orientations are positioned inside the beam using tie constraints and position constraints. Twenty-node linear brick elements under a full integration scheme were used to model the concrete beams. In addition, a separate beam as numerically simulated only with surface-mounted PZT patches, so orientation effects were not considered. These PZT patches were directly attached to the beam surface with surface-based tie constraints by keeping the PZT surface as the master surface. The bottom surface of the PZT patch was maintained at zero voltage electric potential throughout the analysis. Corresponding to the experimental procedure, a 100 kHz, 3.5-cycles sinusoidal wave was also applied to the actuator. The beams were analyzed under dynamic implicit analysis with free boundary conditions. Because the analysis was linear, it was difficult to avoid contour spikes even with a reduced integration scheme with hourglass-control. As a consequence, the mesh was later refined, and the analysis was conducted with a full integration scheme. Therefore, the concrete beam was also modelled with 2.5-mm elements. The analysis was executed for a full duration of 0.0003 sec at increments of 1×10^{-6} sec. The time and history outputs were also obtained at approximately the same intervals. As for the experimental investigation, the excitation and response signals were recorded for each case.

Note that dynamic implicit analysis is not the most efficient method for such investigations. However, if dynamic explicit analysis is used, the time increment (Δt) must be sufficiently small to obtain satisfactory results (Markovic et al. 2015). Otherwise, the solutions produced by the dynamic explicit analysis will have a higher error percentage than a dynamic implicit analysis for

the same Δt. So to get a better idea of wave propagation, dynamic implicit analysis was used for the present study. Future studies will need to use alternative methods to increase the computational efficiency of the FE model.

3.6 Structural Health Monitoring Technique

Excitation and response signals were obtained for each case, from both the experimental and numerical studies. The time of flight (ToF) was obtained as the arrival time between the peaks of the excitation and response signals. The type of the signal used varied as the first R-wave package for the surface-mounted PZT patch system and the first S-wave package for the embedded PZT cement module system of propagating waves. A graphical representation of the ToF for the first S-wave package of B#1 (with the embedded PZT cement module of 0^o orientation) from the experimental investigation is shown in figure 3.12. However, the clarity of the propagating wave was affected by noise in the concrete beams. Sometimes it was quite difficult to directly capture the peak of the relevant response signal. Therefore, to identify the peak of the output signal, the signal energy of the propagating elastic stress waves was utilized. The signal energy (E_s) as a function of signal energy density distribution S(t) is defined in equation (3.2). S(t) is defined in the time domain, and it is the distribution of input/output signal. At instances where this approach was also difficult to implement, a number of crests were used to manually obtain the peak of the required wave package.

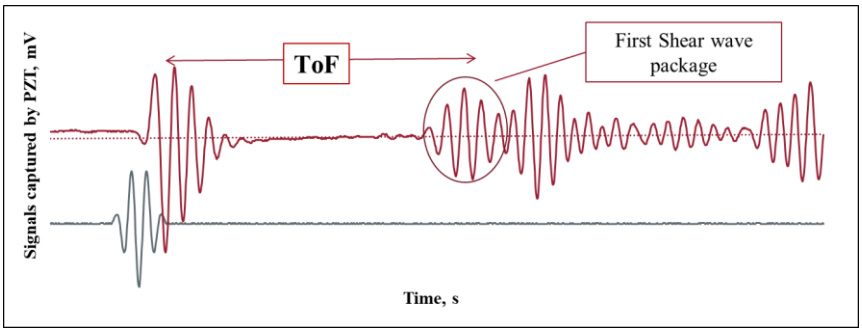

Figure 3.12 The ToF of the first S-wave package of B#1 (with the embedded PZT cement module of 0^o orientation)

$$E_s = \int |S(t)|^2 \, dt \tag{3.2}$$

The relationship between the ToF and the modulus of elasticity of the material (Rose, 1999) is depicted in equations (3.3) to (3.6). These equations are only valid under the assumption of concrete being an isotropic and homogenous medium. They further assume that the lateral dimension of the beam is relatively large in comparison to the propagating wave. As the first S-wave package was being utilized, the effect from the boundary reflected waves was not taken into consideration in either the experimental investigation or the FE model. As shown in figure 3.12, the first S-wave package obviously traveled from the actuator to the sensor, and the distance between them were known. The following equations were used to calculate the WMoE of the concrete in the experimental investigation utilizing either the first S-wave package in the embedded PZT cement module system or the first R-wave package in the surface-mounted PZT patch system.

$$C_s = {}^{l}/_{ToF} \tag{3.3}$$

$$C_s = \sqrt{\frac{E}{2(1+\nu)\rho}} \tag{3.4}$$

$$C_R = \left(\frac{0.87+1.12\nu}{1+\nu}\right) \times \sqrt{\frac{E}{2(1+\nu)\rho}} \tag{3.5}$$

$$ToF \propto \frac{1}{C_s (or\ C_R)} \propto \frac{1}{\sqrt{E}} \tag{3.6}$$

where

C_S is the S-wave velocity,

C_R is the R-wave velocity,

E is the wave modulus of elasticity (WMoE) obtained on the basis of either the S-wave propagation (via the embedded PZT cement modules) or the R-wave propagation (via the surface-mounted PZT patches),

ToF is the time of flight (the arrival time between the peaks of the excitation and response signals (either S-wave or R-wave),

ρ is the density of concrete,

v is the Poisson's ratio, and

l is the distance between actuator and sensor.

To calculate the WMoE, the Poisson's ratio and density of concrete given in table 3.5 were used in equation (3.4) with the S-wave velocity and and in equation (3.5) with the R-wave velocity.

Chapter 4 Results and Discussion

In this chapter, the results from the experimental tests and numerical FE analysis conducted on the concrete beams and panel are presented and analyzed, with emphasis on determining the WMoE using the surface-mounted PZT patch system and the embedded PZT cement module systems and comparing the two systems.

4.1 Basic Material Properties of the Concrete

The average measured slump for the desirable mixture was approximately 125 mm, with a density of 2,400 kg/m^3. The static modulus of elasticity (SMoE) and compressive strength obtained from the cylinder compression test were measured at 7 days, 14 days, and 28 days to study the development of both stiffness and strength with age. The mean values of the three replicates for the compressive strength and SmoE, along with their variations at certain ages, are summarized in table 4.1. The 28-day compressive strength and SMoE of concrete used were 45 MPa and 24.1 GPa, respectively. Because of the additions of silica fume and GGBFS, approximately 70 percent of the 28-day strength had been gained by 7 curing days and 85 percent by 14 curing days.

Table 4.1 Material properties of the concrete by compression test

Age, day	f_c', MPa	COV	SMoE, GPa	COV
7	31.3	4%	19.09	9%
14	37.6	6%	21.41	3%
28	45.9	3%	24.14	2%

4.2 Results from the Experimental Investigations on the Concrete Beams

4.2.1 Optimum Wave Frequency

Because the wave frequency has a significant effect on the velocity and energy of a wave during propagation, some trial experiments with varying wave frequencies were first conducted to find the optimum wave frequency. The idea was to obtain the optimum wave frequency under which the peaks of S-waves from the embedded PZT cement module system and peaks of R-waves from the surface-mounted PZT patch system were more clearly visible. As an example, the response signals of B#1 with the embedded PZT cement modules of 0^o orientation at 10 days were obtained over a frequency range of 80 kHz to 180 kHz, with an increment of 20 kHz. The results of the selected wave frequencies are shown in figure 4.1. At low wave frequencies (such as 80 kHz), the S-wave package was not easy to distinguish from the subsequent reflective waves from the boundaries because of the low wave velocity. If the wave frequencies were very high (such as 140, 160, and 180 kHz), the amplitude of the S-wave package was relatively lower, as depicted in figure 4.1(d)-(f). The response at 100 kHz showed the best characterization among all scenarios tested. Therefore, a 100-kHz wave frequency was eventually chosen to obtain the clearest waveforms. It was also observed that the respective wave velocity increased as the frequency of the propagating wave increased, and thus, the corresponding ToF decreased.

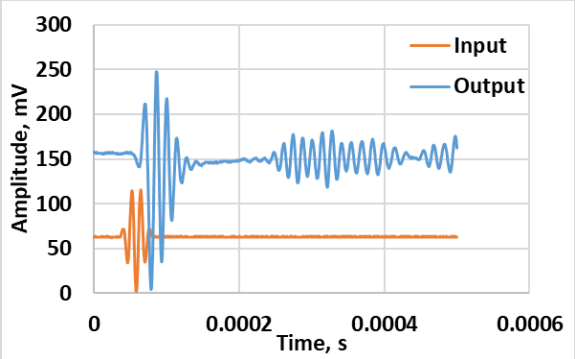

(a) 80 kHz

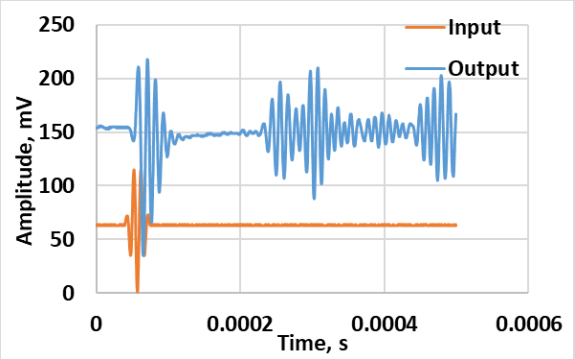

(b) 100 kHz

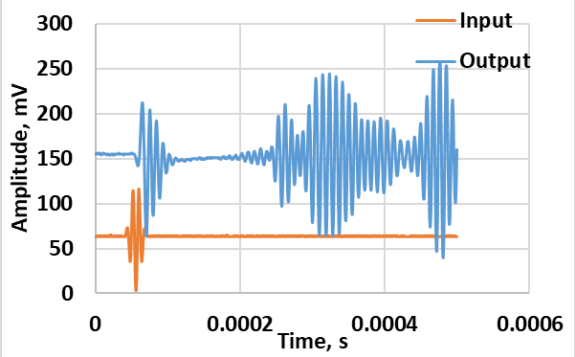

(c) 120 kHz

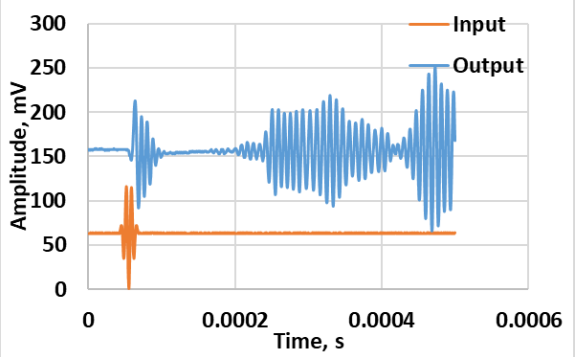

(d) 140 kHz

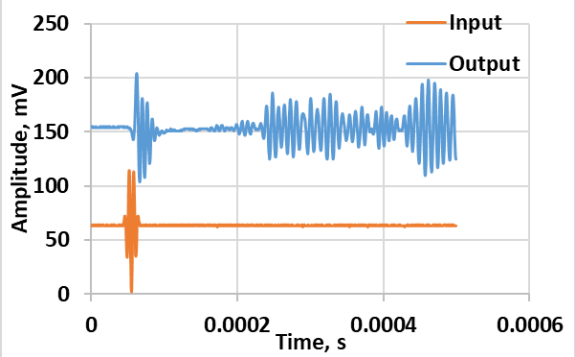

(e) 160 kHz

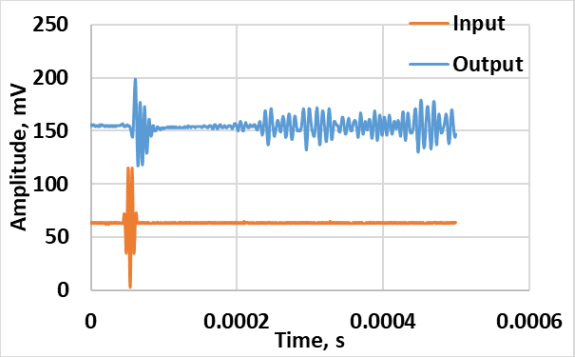

(f) 180 kHz

Figure 4.1 Response signals from the embedded PZT cement module system at different frequencies of B#1 at the age of 10 days

Similarly, some trial experiments with varying wave frequencies were conducted to find the optimum wave frequency at which the surface-mounted PZT patch system could effectively observe/pick up the R-wave packages from the response signals. The response signals of B#1 with the surface-mounted PZT patches at 10 days were obtained over a frequency range of 80 kHz to 180 kHz, with an increment of 20 kHz. The wave propagations under selected wave frequencies are shown in figure 4.2. At some wave frequencies (such as 80 kHz, 120 kHz, and 140 kHz), the R-wave package merged with the subsequent reflective waves, so it was difficult to identify the peak and determine the ToF. At high wave frequencies (such as 160 kHz and 180 kHz), the amplitude of the R-wave package was relatively lower, so it is also not easy to identify the peak and ToF. However, the response at 100 kHz clearly distinguished the R-wave package for all scenarios tested. Therefore, the wave frequency of 100 kHz was chosen to identify the S- and R-wave packages in the embedded PZT cement modules and surface-mounted PZT patches to determine and compare the WMoE.

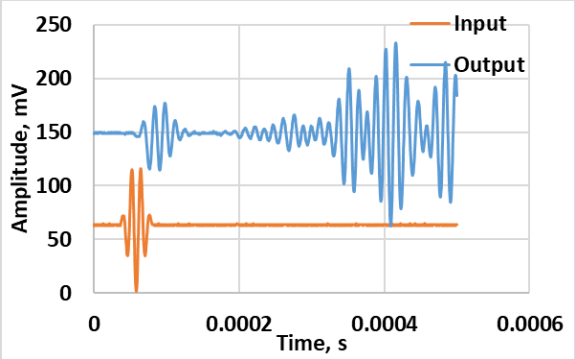

(a) 80 kHz

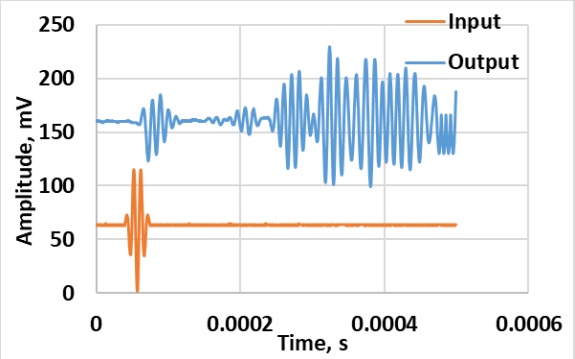

(b) 100 kHz

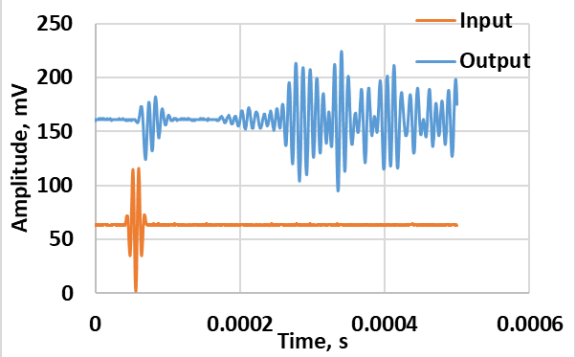

(c) 120 kHz

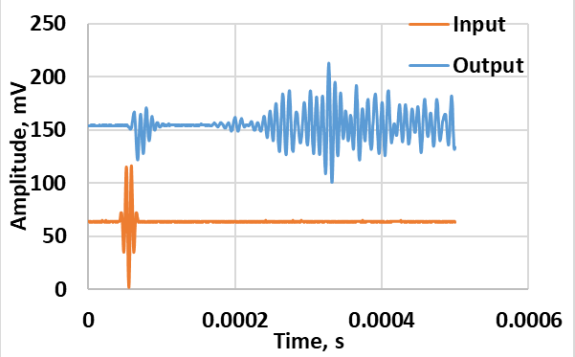

(d) 140 kHz

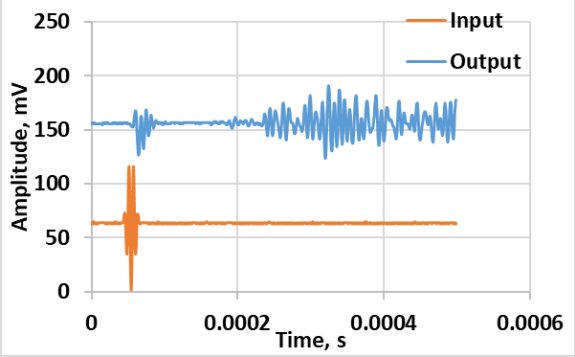

(e) 160 kHz

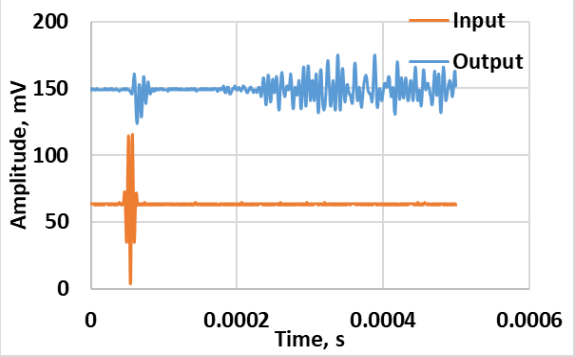

(f) 180 kHz

Figure 4.2 Response signals from the surface-mounted PZT patch system at different frequencies of B#1 at the age of 10 days

4.2.2 Effect of the Orientation of the Embedded PZT Cement Modules

As discussed in Chapter 2, longitudinal wave oscillations occur in the direction of wave propagation and are of a higher velocity and a lower amplitude. In contrast, S-waves oscillate the particle perpendicular to the direction of propagation and are of a higher amplitude and a lower velocity. Therefore, S-waves are frequently adopted for ultrasonic techniques. Also, because the S-waves excited by PZT are usually perpendicular to the direction of propagation, it is important to investigate the effects of the orientation of the embedded PZT cement modules on wave transformation.

Wave analysis testing was performed with the embedded PZT cement modules in three concrete beams with three different orientations: $\theta = 0^{o}, 45^{o}, 90^{o}$. Again, understanding the optimum orientation of the PZT cement modules or the effects of the orientation of the PZT cement modules on the propagating waves would be beneficial to successfully implement the WMoE tests. The excitation and response signals of the three beams with the embedded PZT cement modules at 10 days were obtained at a constant frequency of 100 kHz, as depicted in figure 4.3. As shown in figure 4.3(a), at an orientation of 0^{o} (B#1), the first S-wave package with a higher amplitude was obviously distinguished from the leading longitudinal wave with low amplitude and the later reflective waves. When the orientation of the embedded PZT cement modules increased to 45^{o} (B#2), the first S-wave package could still be distinguished from the leading longitudinal wave, but it partially merged with the following reflective waves, as illustrated in figure 4.3(b). At an orientation of 90^{o} (B#3), the S-wave package partially overlapped with the subsequent reflective waves, thus making the identification of the wave peak quite difficult.

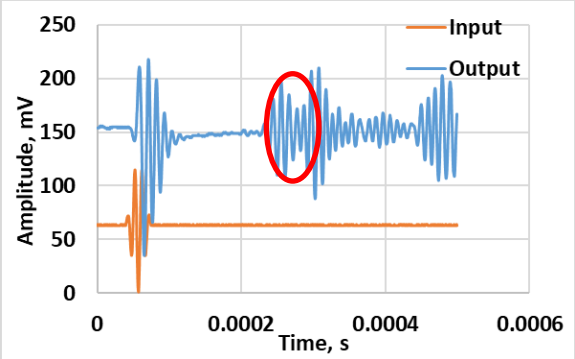

(a) B#1 (θ = 0º)

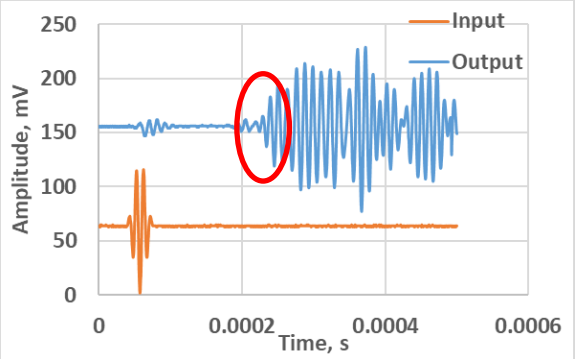

(b) B#2 (θ = 45º)

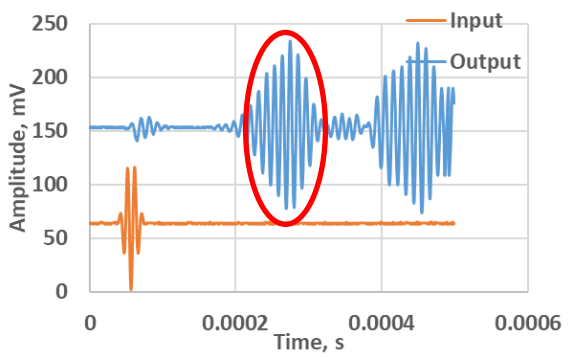

(c) B#3 (θ = 90º)

Figure 4.3 Excitation and response signals from the embedded PZT cement module systems with different orientations at the age of 10 days

4.2.3 Determination of the ToF and WMoE

The ToF of the first S-wave package from B#1 and B#2 were determined from the excitation and response signals of the embedded PZT cement modules by utilizing the peak of the propagating waves. However, the peak identification of the first S-wave package in B#3 was difficult because it merged with the waves. It appeared that if the most apparent peak of the whole wave package (circled in figure 4.3(c)) was utilized in determining the WMoE, then the results would highly deviate from the actual measurement. It was reasonable to assume that the wave peak shifted right because of wave merging. As mentioned in Chapter 2, the S-wave package is the second to arrive, following the longitudinal wave package. Therefore, to avoid larger errors, the

peak of the second wave package in figure 4.3(c) was obtained manually by utilizing the number of crests in each wave package from the response signal data. After determination of the ToF, the WMoE of the concrete beams was calculated by using equation (3.5). The variations in the WMoE estimations versus the age of the concrete, along with the mean values of the three beams, are shown in figure 4.4. During the first week of cement hydration, a rapid increase in the WMoE was observed, followed by a slower increasing rate of WMoE. This behavior corresponded to the early age strength gain of the concrete. At 7 days, B#1 had a WMoE of 17.59, B#2 a WMoE of 18.58, and B#3 a WMoE 16.60 GPa. After 28 days, B#1 had a WMoE of 25.81,, B#2 a WMoE of of 25.96, and B#3 a WMoE of 24.91 GPa. The experimental results of the three beams with differently oriented PZT cement modules indicated that at 28 days, B#2 ($\theta = 45^{o}$) had the highest WMoE, followed by B#1 ($\theta = 0^{o}$), and B#3 ($\theta = 90^{o}$).

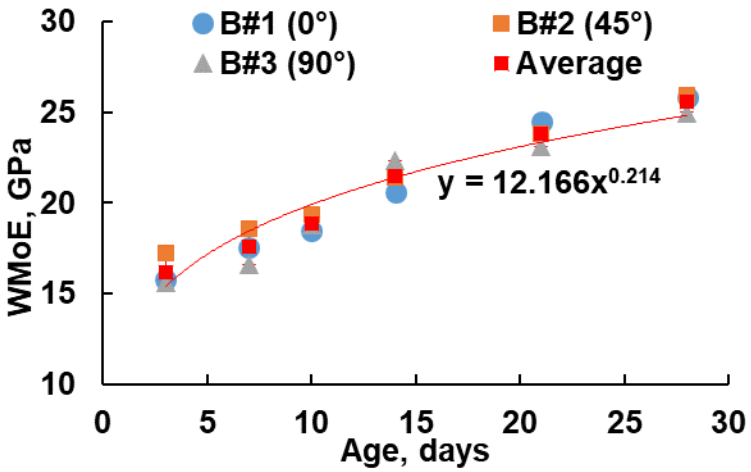

Figure 4.4 Variation of the experimental WMoE versus time after casting

4.2.4 Comparison of the Surface-Mounted PZT Patch System versus the Embedded PZT Cement Module System

Comparisons of the WMoE obtained by the embedded PZT cement module and surface-mounted PZT patch systems at different ages of the concrete beams are shown in figure 4.5 for

B#1 ($\theta = 0^{o}$), figure 4.6 for B#2 ($\theta = 45^{o}$), and figure 4.7 for B#3 ($\theta = 90^{o}$). Regardless of the orientations of the PZT cement modules, the WMoE values determined by the surface-mounted PZT patch system tended to be higher than those from the embedded smart PZT cement module system. It was evident that the largest difference in the WMoE determined by the surface-mounted PZT patches and the embedded PZT cement modules was in B#3, followed by B#1 and then B#2. The test results on B#2 indicated the lowest difference. However, the difference between the two system measurements became smaller as the concrete aged, indicating that the concrete exterior surfaces gained strength and stiffness more quickly than the interior. The surface-mounted PZT patch system measured the concrete surface properties within one wavelength depth, whereas the embedded PZT cement module system detected and represented the WMoE for the interior of the concrete. As summarized in table 4.2, at 7 days, the variations in the estimated WMoE values between the two systems were approximately 10.3 percent for B#1, 0.16 percent for B#2, and 20.5 percent for B#3 . The WMoE values of the exterior concrete measured by the surface-mounted PZT patches were always higher than the values for the interior concrete acquired by the embedded PZT cement modules, indicating the fast curing of the exterior concrete near the beam surface. At the reference age of 28 days, the variations decreased to approximately 3.7 percent for B#1, 2.5 percent for B#2, and 3.3 for B#3, implying that the interior and exterior concrete were fully cured. It was also observed that the coefficient of variation (COV) of the WMoE among the three beams determined by the surface-mounted PZT patch system was lower than the determination produced by the embedded smart PZT cement modules. In other words, the surface-mounted PZT patch system produced a more consistent WMoE measurement.

Note that the surface-mounted PZT patch system is more applicable to existing structures, as the installation procedures for PZT patches on a hardened concrete surface are more controlled

and reliable. Because the location, distance, and orientation are more accurate and not of concern for the surface-mounted PZT patch system, the WMoE evaluation is more consistent and accurate.

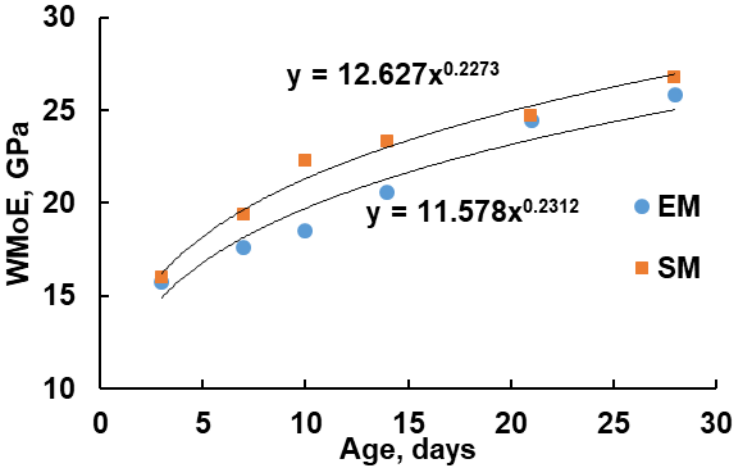

Figure 4.5 Experimentally measured WMoE versus time of casting for B#1 (0º)

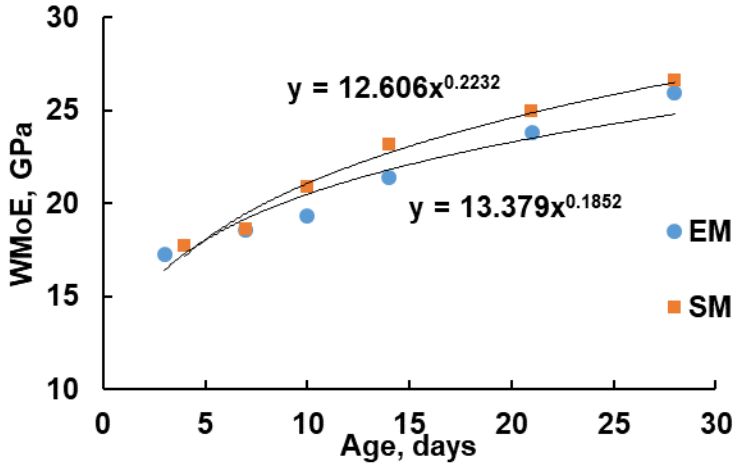

Figure 4.6 Experimentally measured WMoE versus time of casting for B#2 (45º)

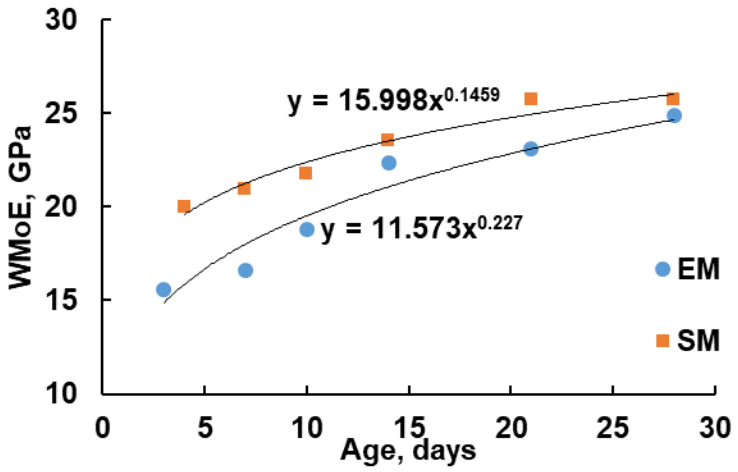

Figure 4.7 Experimentally measured WMoE versus time of casting for B#3 (90º)

Table 4.2 WMoE data determined by the embedded PZT cement module and surface-mounted PZT patch systems

Beam	7 days			28 days		
	Embedded (GPa)	Surface-mounted (GPa)	Difference (%)	Embedded (GPa)	Surface-mounted (GPa)	Difference (%)
B#1	17.59	19.41	10.3	25.81	26.75	3.7
B#2	18.58	18.61	0.16	25.96	26.60	2.5
B#3	16.60	20.95	20.5	24.91	25.74	3.3

4.3 Results from the Numerical Analysis

4.3.1 Results from the FE Model of PZT Cement Modules

The undeformed configuration of a PZT cement module and its deformed configuration after linear electric input are displayed in figures 4.8(a) and 4.8(b), respectively. The figure illustrates the ability of the PZT patch to deform the cement casing in the presence of an external electric potential. The electric potential distribution of the system is shown in figure 4.8(c). As demonstrated in figure 4.8, the electric potential was only relevant to the area occupied by the PZT. ABAQUS treats the electric potential as a separate degree of freedom (DOF). In ABAQUS terminology, it is defined as the 9^{th} DOF. The existence of such a localized DOF, which is only

confined to a part of the structure, creates complications in the numerical FE modelling due to compatibility issues. In other words, the PZT had an extra DOF that was not present in the rest of the concrete structure. As expected, the rest of the area had an electric potential of 0 V. The displacement contours (u3) in direction 3 (z direction, i.e., through the thickness of the PZT patch) due to the deformation of the module are shown in figure 4.8(d). The results were similar to the findings reported by Markovic et al. (2015).

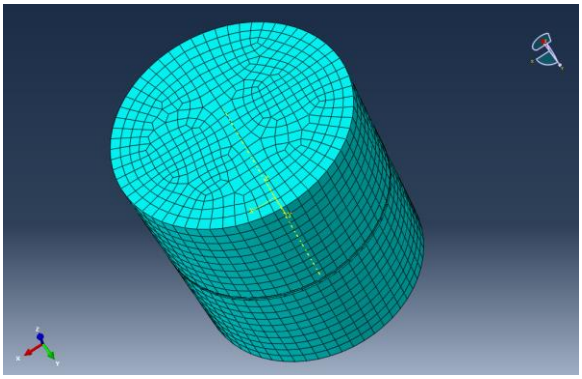

(a) Original configuration

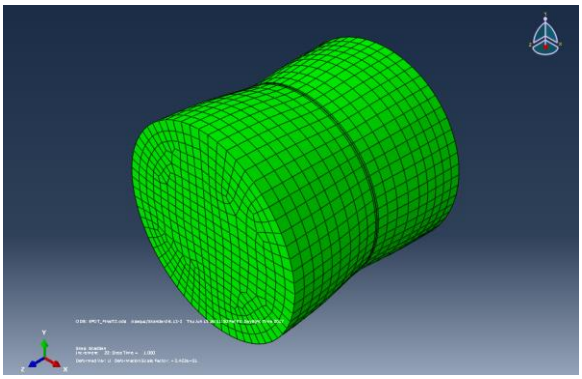

(b) Deformed configuration

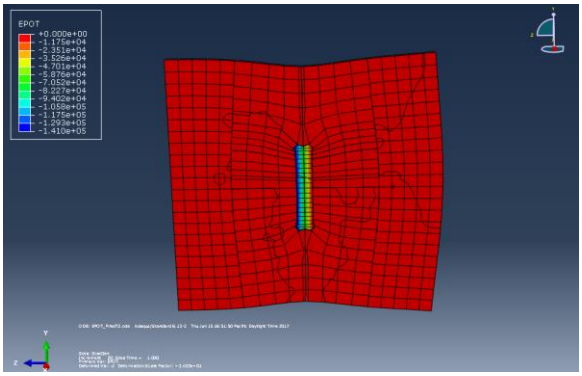

(c) Electric potential distribution

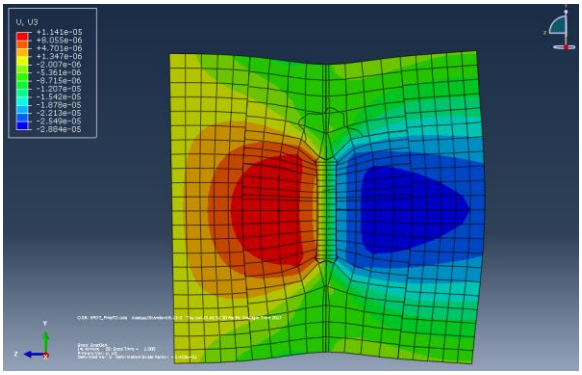

(d) Displacement field contour

Figure 4.8 Results of the FE simulation of the PZT cement module

The relationship between a linear electric input and the response in terms of displacement in the 3rd direction (z direction) is plotted in figure 4.9. As shown in figure 4.9, there was a linear relationship between the displacement component u3 and the input of the electric potential. As indicated, the response was sensitive to the sign of the applied signal. As the load was applied in the negative direction with respect to the global axis system, there was a negative displacement field output. This trial run was conducted to verify the functionality of the FE model. As expected, the sensor response varied linearly with a given linear electric input.

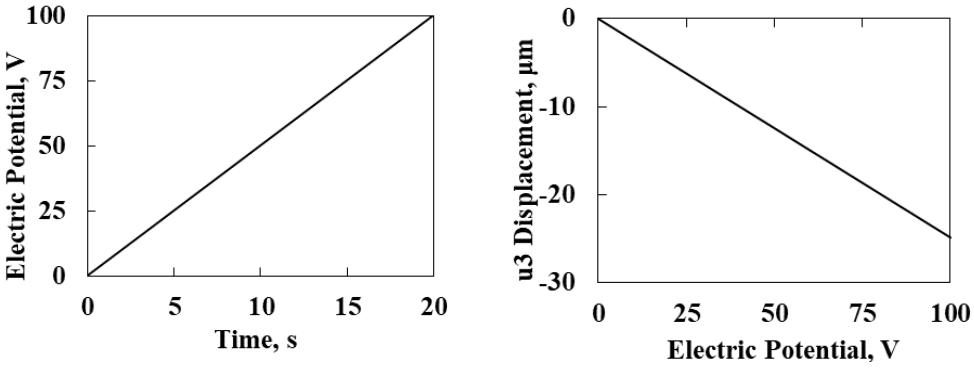

Figure 4.9 Linear input signal and the corresponding displacement output from the FE model of PZT cement module

4.3.2 Results from the FE Analysis of the Wave Propagation in Beams

A numerical analysis was performed with the embedded PZT cement module system for each orientation ($\theta = 0^o$, 45^o, or 90^o) to verify the concept of S-wave propagation used in the study. Assigning appropriate constraints to the model while maintaining efficiency in computation performance is one of the main difficulties in dealing with this kind of numerical simulation. The incompatibility of the 9^{th} DOF was also emphasized here. Trial runs were performed with altering mesh parameters in ABAQUS, such as the linear incompatible elements, full integration schemes with refined meshes, selective refined meshes, and reduced integration with coarse meshes. However, the most efficient method with comparable results was the full integration scheme with a slightly refined mesh. The selective refined mesh was used on the slave surfaces of the surface-based tie constraints.

The displacement contours from the dynamic implicit analysis of the FE models of concrete beams are displaced in figures 4.10 to 4.13 for B#1 ($\theta = 0^o$ orientation of the embedded PZT cement module), B#2 ($\theta = 45^o$ orientation of the embedded PZT cement module), and B#3 ($\theta = 90^o$ orientation of the embedded PZT cement module), respectively. The three subfigures in figure 4.10 to 4.13 depict the counters of magnitude of global displacement, u2 displacement along the y

direction, and u3 displacement along the z direction, respectively. For B#1 and B#3 with PZT cement module orientations of 0º and 90º, the u2 displacement component was much higher than the u3 displacement component at a given time. However, the displacement vector u2 produced displacement contours with a greater intensity than the u3 displacement component. In contrast, for B#2 with a PZT cement module orientation of 45º, the u2 and u3 displacement contour intensities were closer to each other. Thus, there was not much distinction between the P-wave and S-wave in this case. These variations could be further observed when the signal patterns were analyzed.

The displacement contours produced by the surface-mounted PZT patch system are shown in figure 4.13. The penetration depth of the propagating wave from the surface to the interior of the concrete beam was lower than those shown in figures 4.10 to 4.12 for the embedded PTZ system. As expected, the wave patterns tended to be propagated near the surface of the concrete beam in the surface-mounted PZT patch system because R-waves usually penetrate up to only one wavelength in depth from the surface of structures. In addition, it is evident from figure 4.13 that the R-wave package (denoted by the u2 displacement component) was much higher than the propagating P-wave package (denoted by the u3 displacement component).

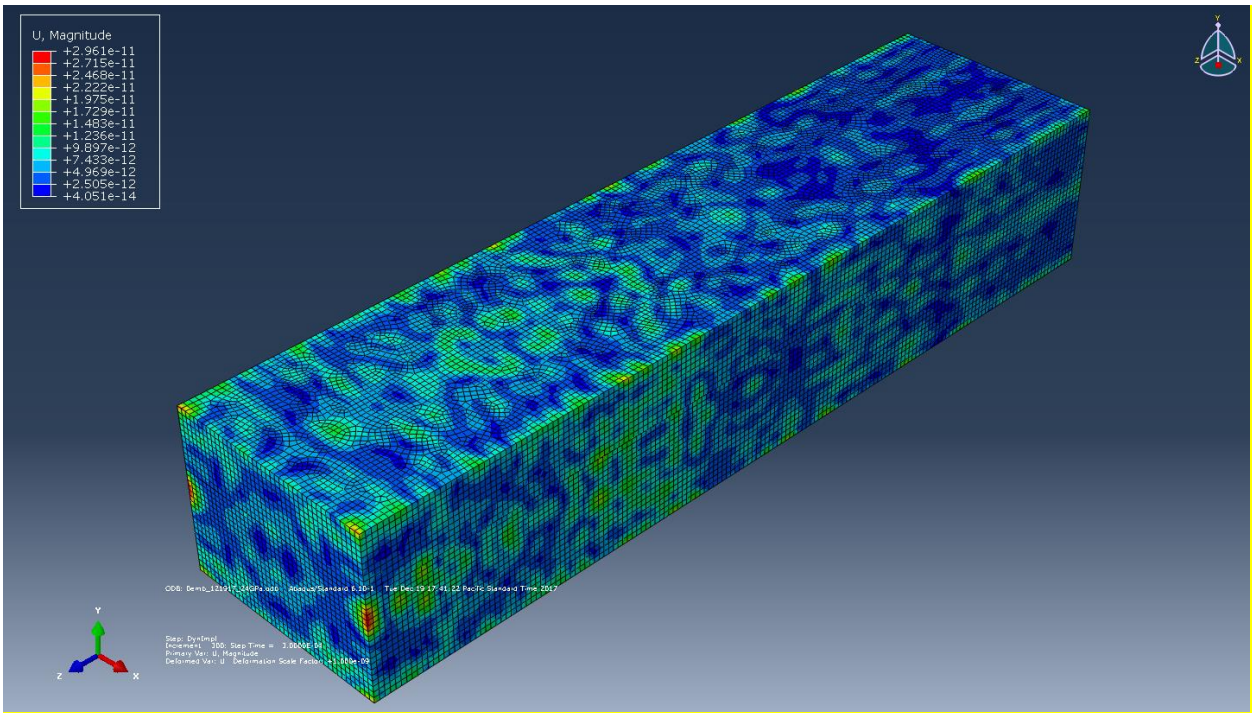

(a) Displacement contours (u magnitude)

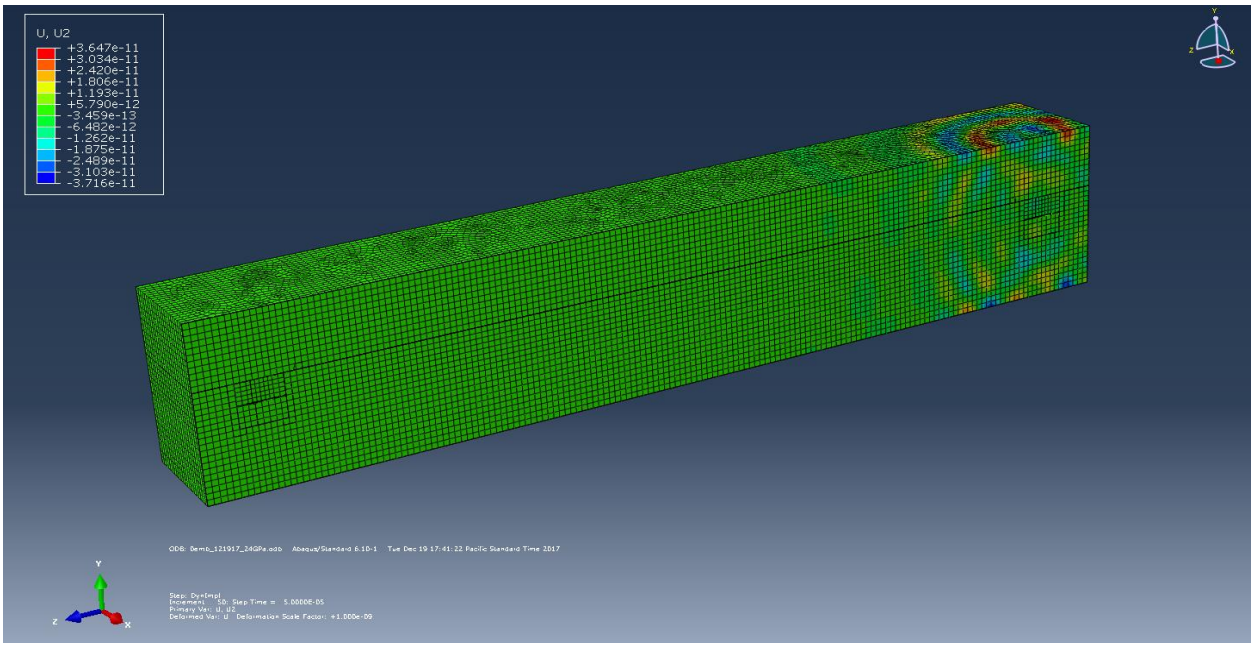

(b) Contours of vector u_2 at a given time frame along the y-z plane

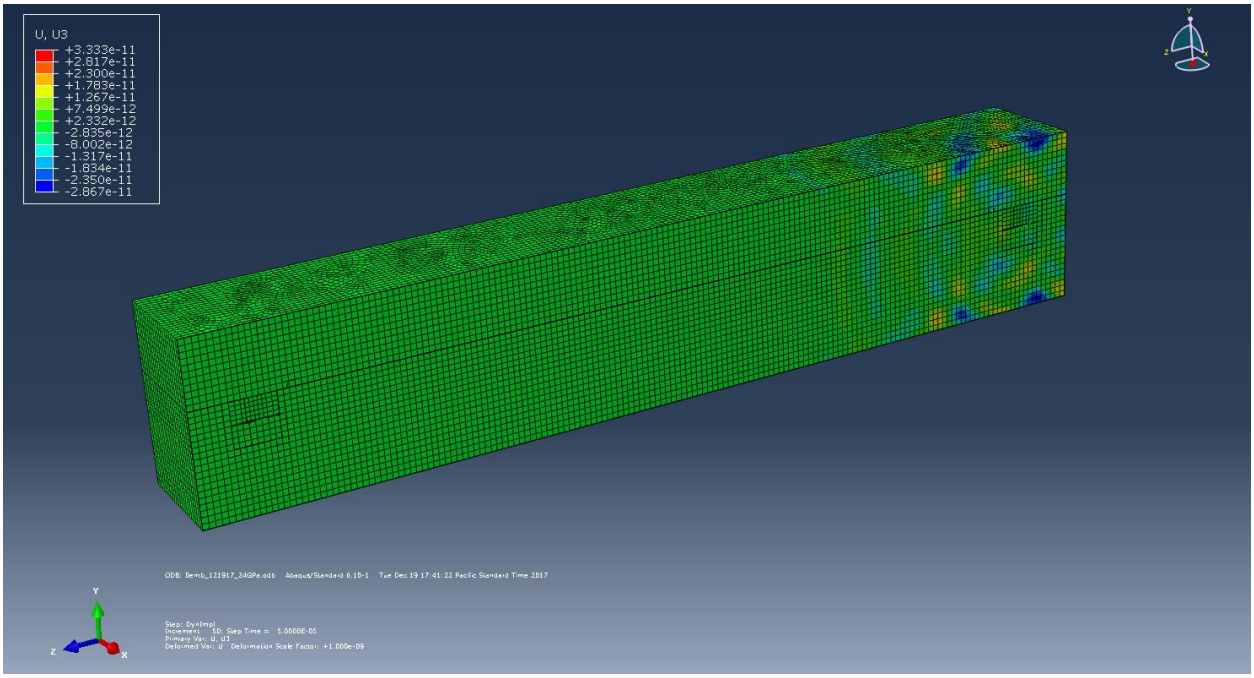

(c) Contours of vector u3 at a given time frame along the y-z plane

Figure 4.10 Displacement contours from the FE analysis of B#1 ($\theta = 0^{o}$) with embedded PZT cement modules

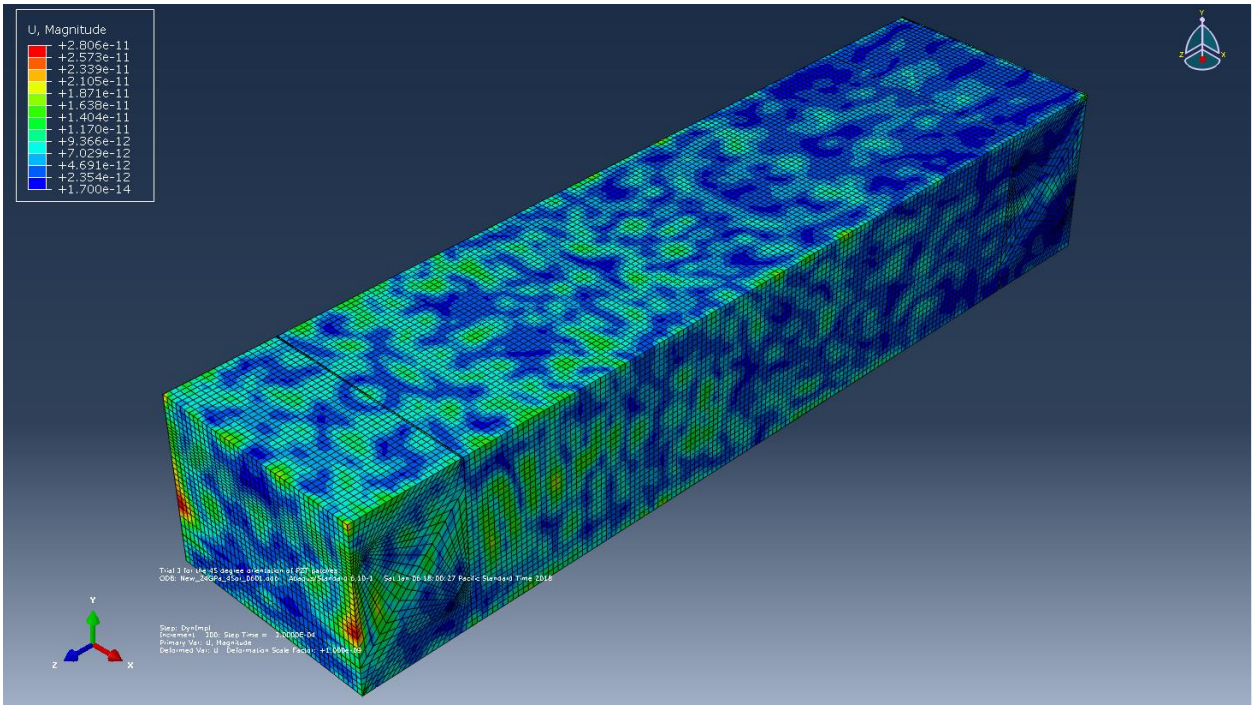

(a) Displacement contours (u magnitude)

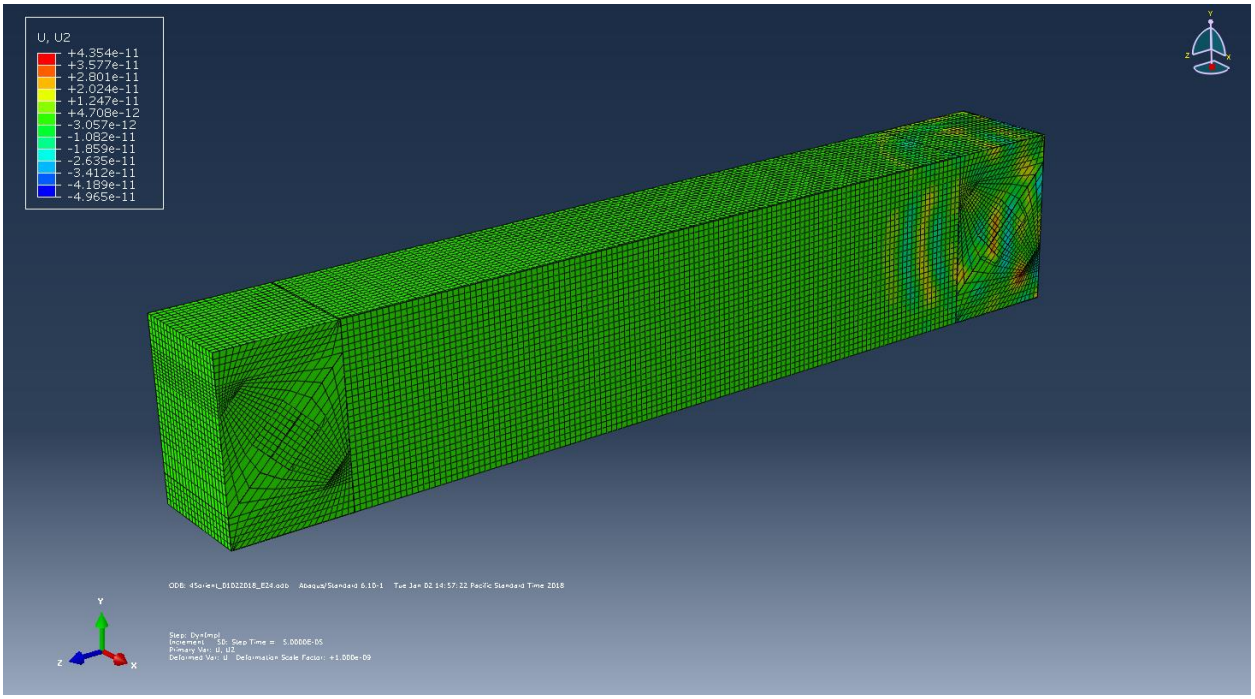

(b) Contours of vector u_2 at a given time frame along the y-z plane

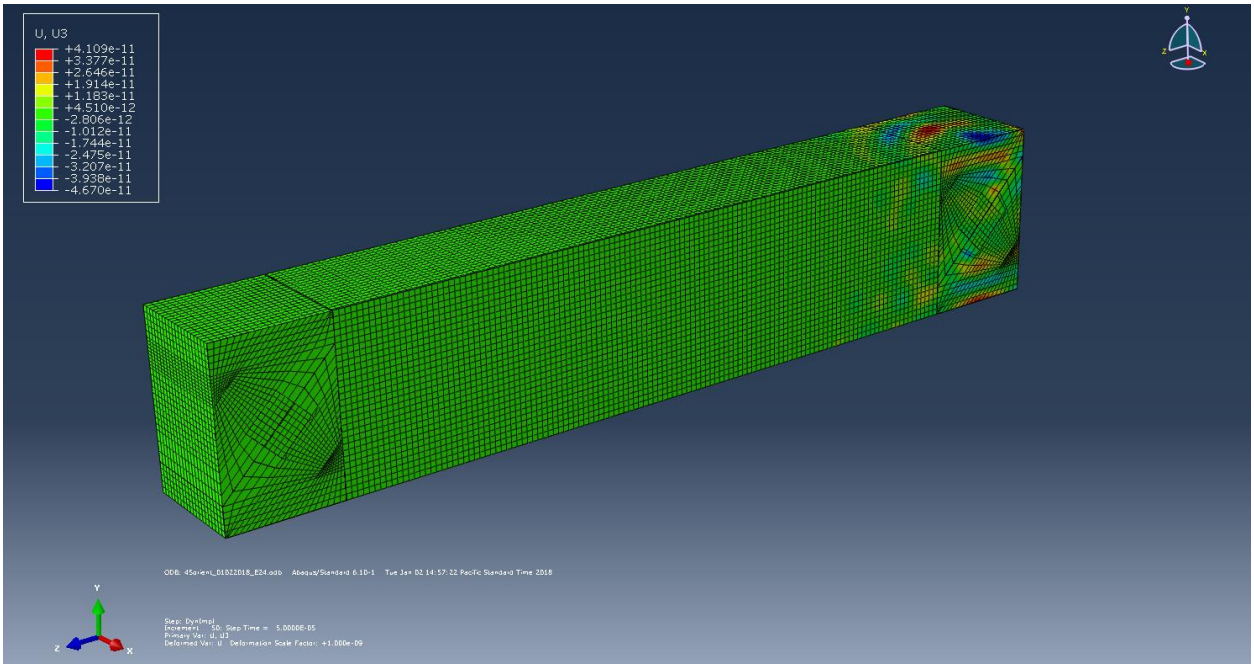

(c) Contours of vector u_3 at a given time frame along the y-z plane

Figure 4.11 Displacement contours from the FE analysis of B#2 ($\theta = 45^{o}$) with embedded PZT cement modules

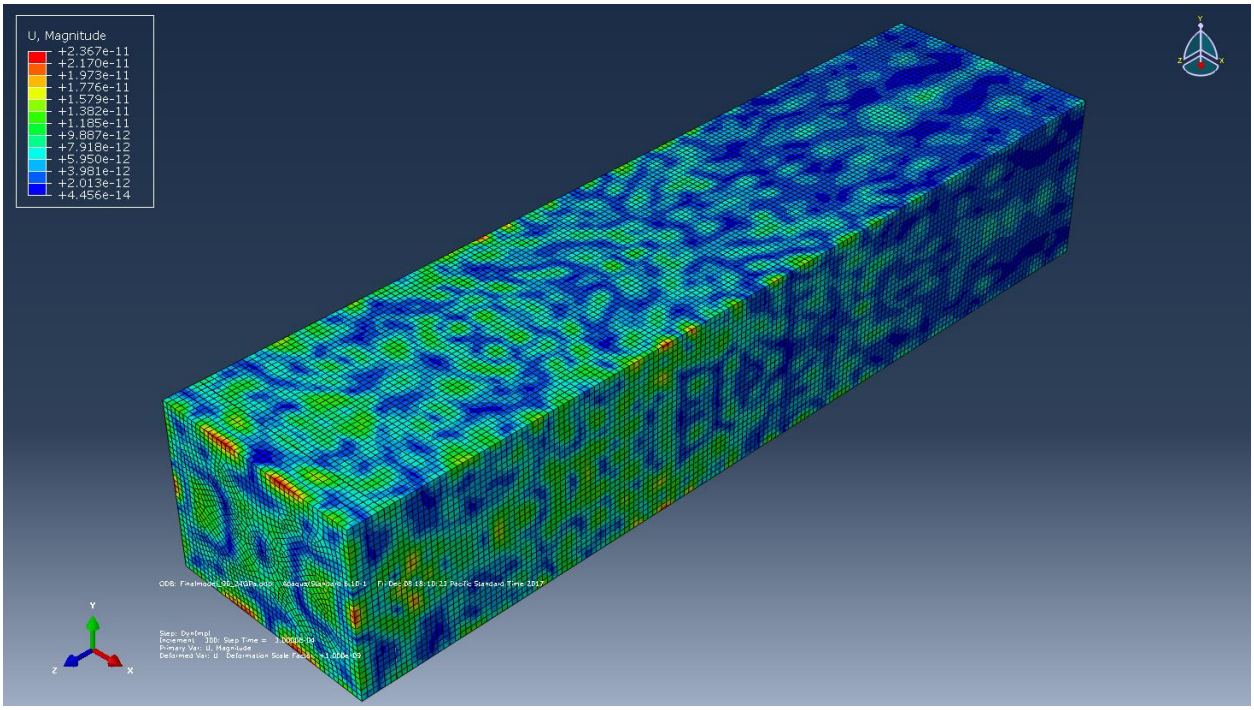

(a) Displacement contours (u magnitude)

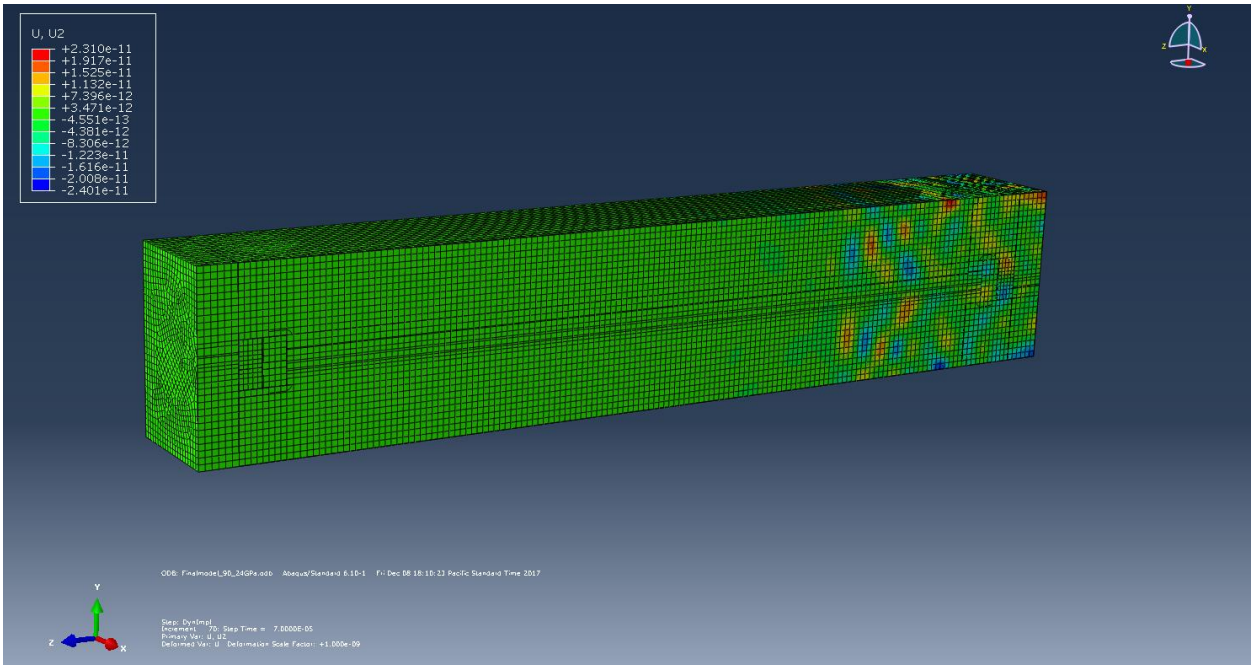

(b) Contours of vector u_2 at a given time frames along the y-z plane

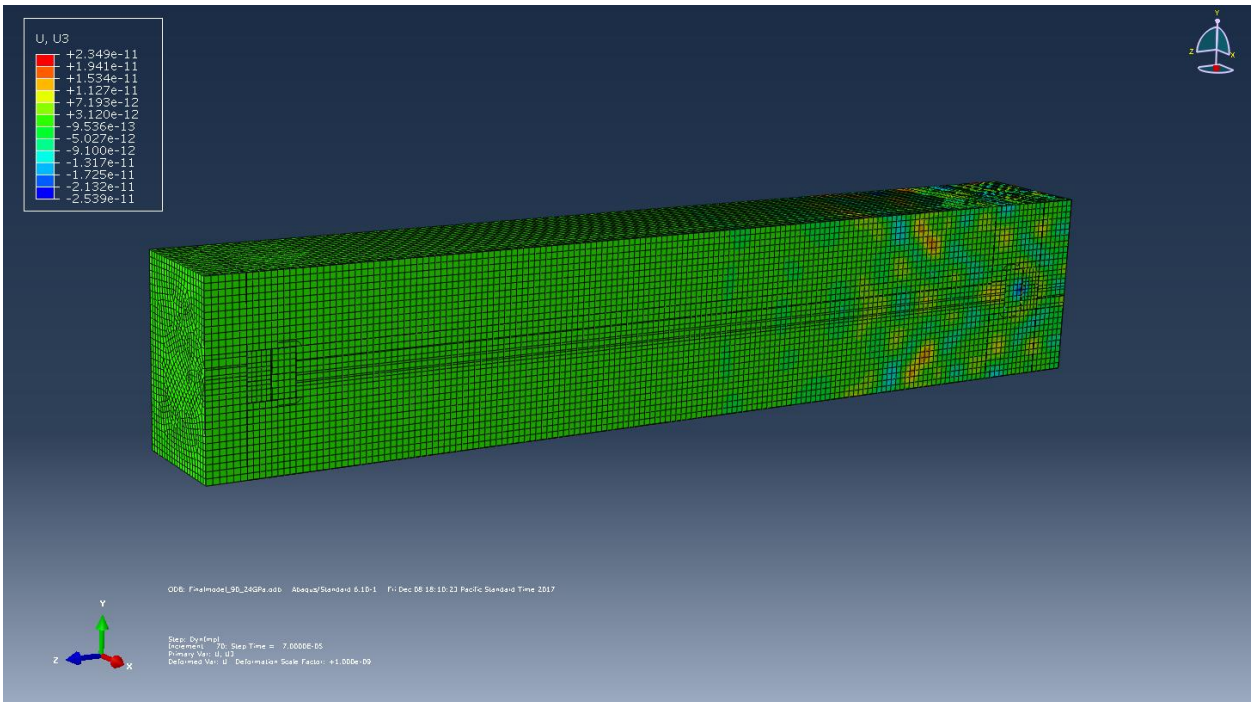

(c) Contours of vector u_3 at a given time frames along the y-z plane

Figure 4.12 Displacement contours from the FE analysis of B#3 ($\theta = 90^{o}$) with embedded PZT cement modules

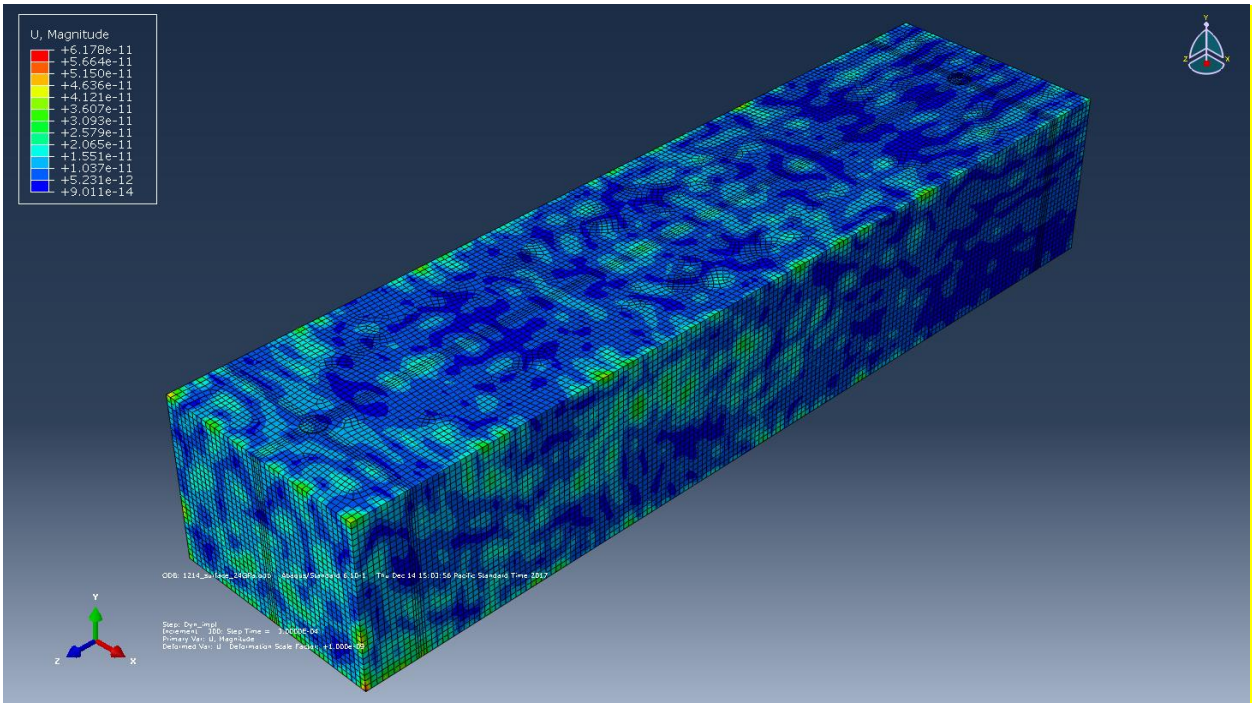

(a) Displacement contours (u magnitude)

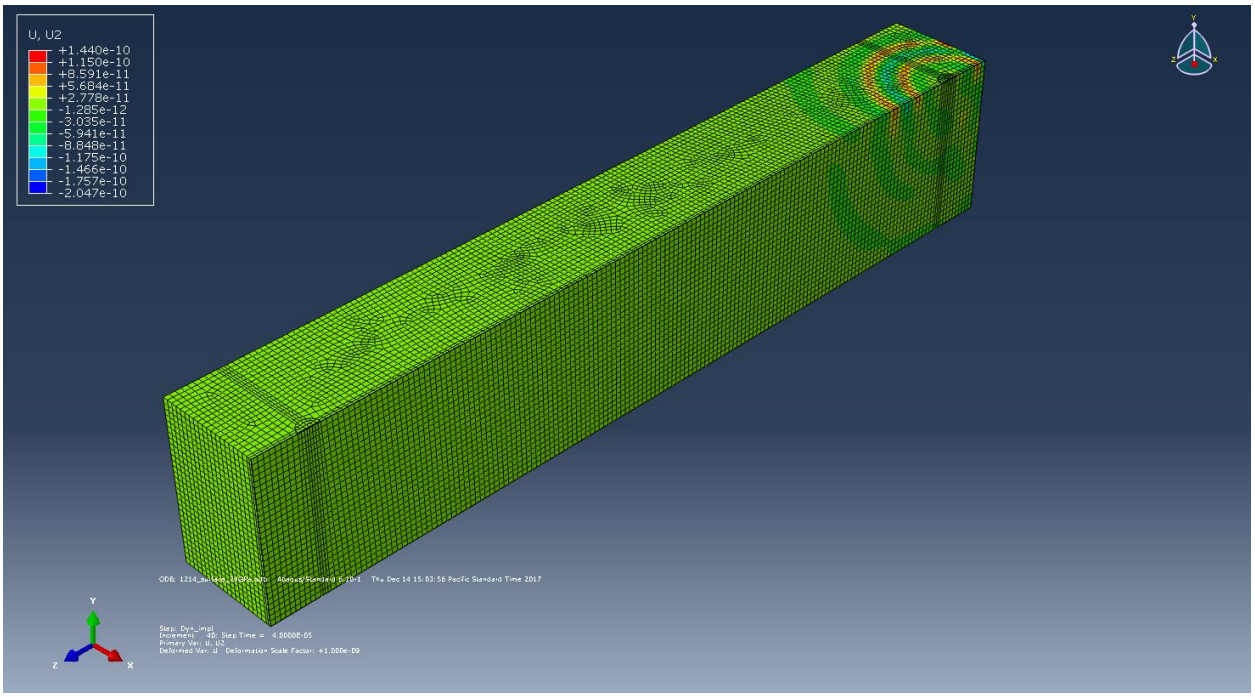

(b) Contours of vector u_2 at a given time frames along the y-z plane

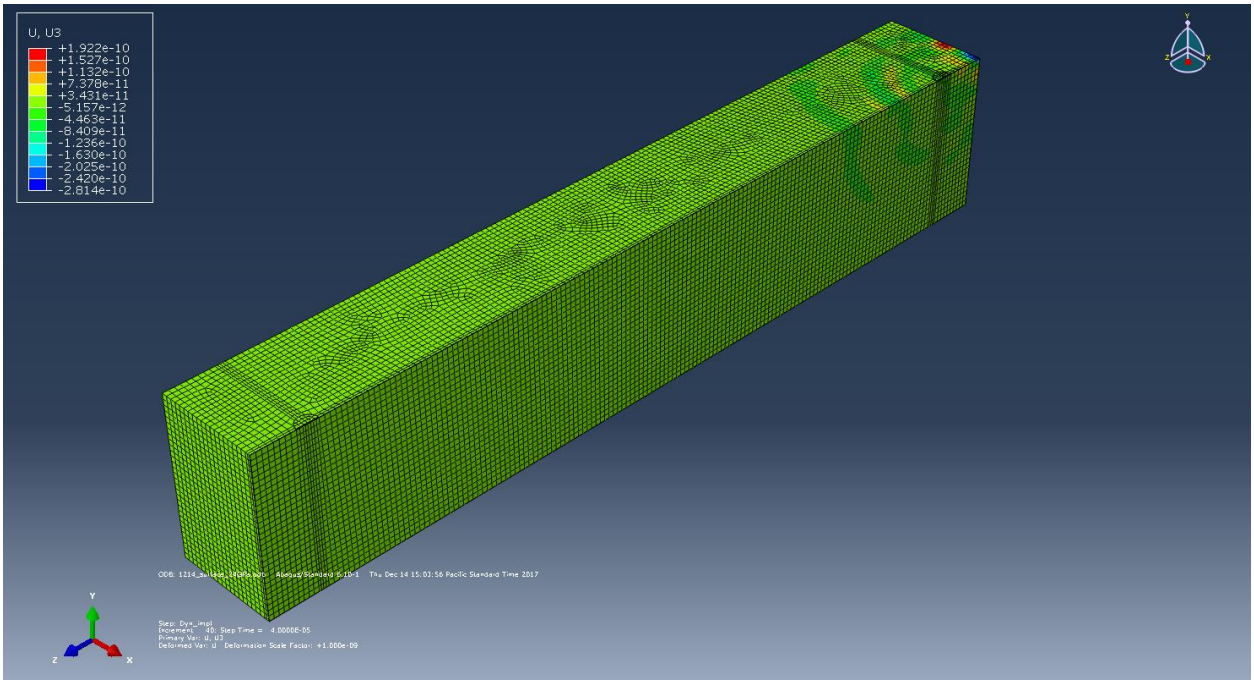

(c) Contours of vector u_3 at different time frames along the y-z plane

Figure 4.13 Displacement contours from the FE analysis of beam with the surface-mounted PZT patches

The excitation signal used for the FE analysis is shown in figure 4.14, while the response signals from the FE analysis and calculated signal energy density distribution for B#1 to B#3 are illustrated in figure 4.15 to figure 4.17. The time corresponding to the peaks of the excitation and response signals are shown by the dotted vertical lines, which are also used to determine the ToF. It is important to note that the wave peak can be either on the negative side or the positive side of the y-axis. By using the signal energy, the absolute maximum value was obtained (see figure 4.15(b)). Thus, the signal energy plot eliminated the effect from any negative signal response, including the effect from the direction of applied load.

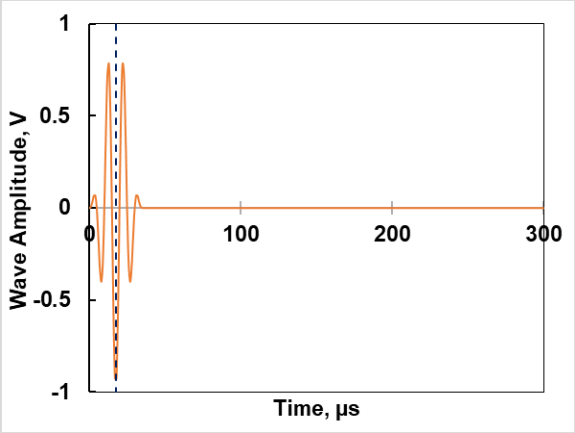

Figure 4.14 Excitation signal of the FE model and its peak

As shown in figures 4.15 to 4.17, the wave peak of the shear wave package was much clearer in the signal energy-time domain than in the wave amplitude-time domain, regardless of the orientation of the embedded PZT modules. As indicated in figures 4.15(a) to 4.17(a), the relevant amplitude peak was not very clearly visible in the wave amplitude-time domain. Then, the signal energy-time domain was used to observe whether there was a clearly distinguishable peak. When $\theta = 45^{o}$, the FE model did not produce a distinguishable wave form in either of the two domains for the embedded PZT cement module system. Therefore, as discussed in the experimental investigation, the wave peak was obtained manually with reference to the number of crests. As shown in figure 4.17, the ToF of the response signal of the $\theta = 90^{o}$ embedded PZT cement module system was obtained with the numerical FE analysis. The wave pattern was clearer than that of the $\theta = 45^{o}$ orientation. However, the signal energy of the $\theta = 90^{o}$ embedded PZT cement module system depicted a more distinguishable variation, which was primarily used to locate the peak of the response signal.

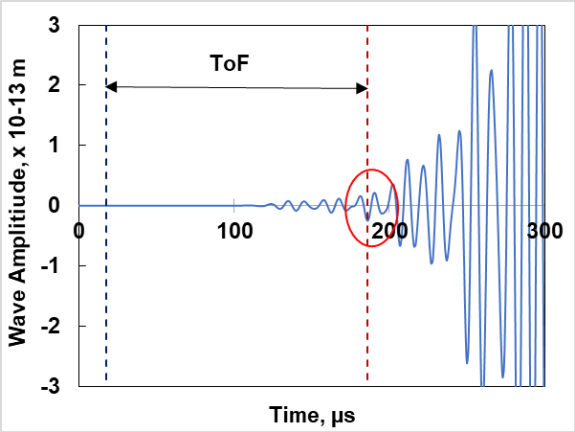

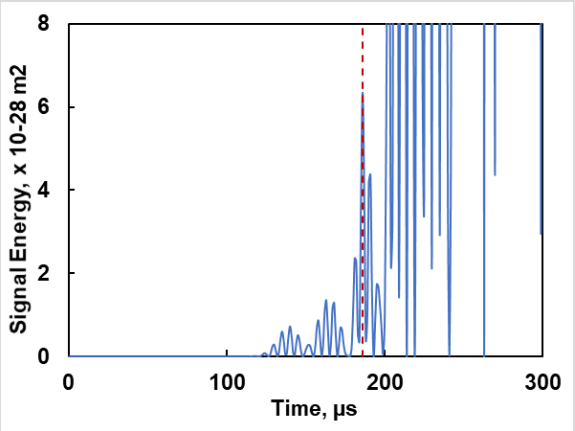

(a) amplitude-time domain (b) signal energy-time domain

Figure 4.15 The first S-wave package from the embedded PZT cement modules in B#1 (0º)

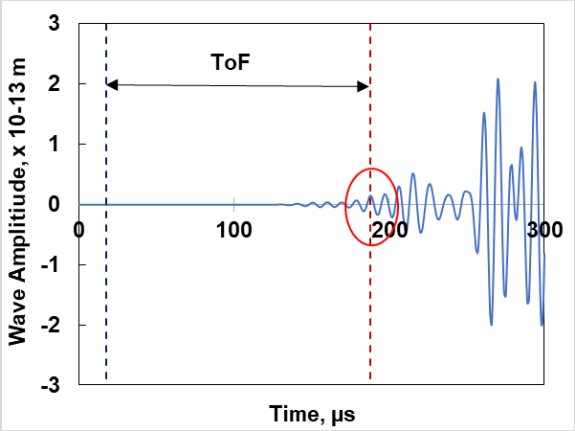

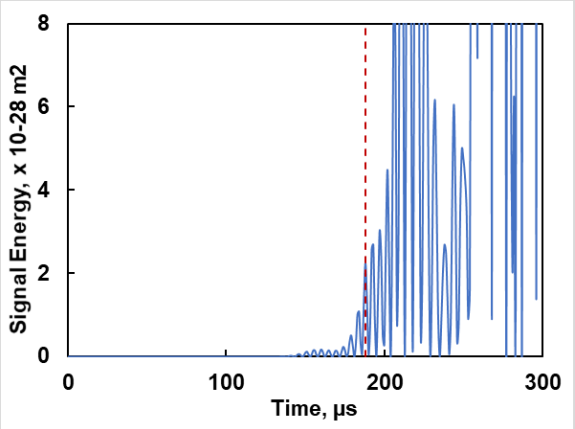

(a) amplitude-time domain (b) signal energy-time domain

Figure 4.16 The first S-wave package from the embedded PZT cement modules in B#2 (45º)

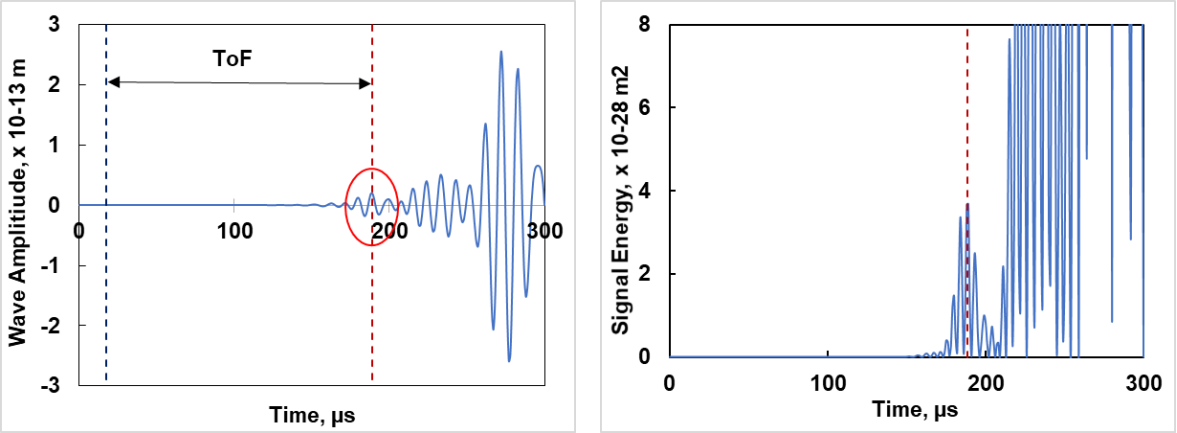

(a) amplitude-time domain (b) signal energy-time domain

Figure 4.17 The first S-wave package from the embedded PZT cement modules in B#3 (90º)

The variations in the signal energy with different orientations of the embedded PZT cement modules are illustrated in figure 4.18. As the orientation changed from 0^0, to 45^0, to 90^0, the peak of the first S-wave package of the response signal shifted from left to right, indicating that the arrival time of the peak postponed as the orientation angle increased. However, the ToF varied in a closer range despite the shift of wave peaks, with increasing orientation of the embedded PZT cement modules with respect to the longitudinal axis of the beam. Furthermore, the signal energy exhibited the maximum magnitude at θ = 0º,and the corresponding wave peak was very clear in the signal energy-time domain. It was followed by the θ = 90º orientation of the embedded PZT cement modules with a slightly lower but clearly distinguishable signal peak. The signal energy at θ = 45º of the embedded PZT cement modules did not show a clear distinction between the rest of the crests and its wave peak.

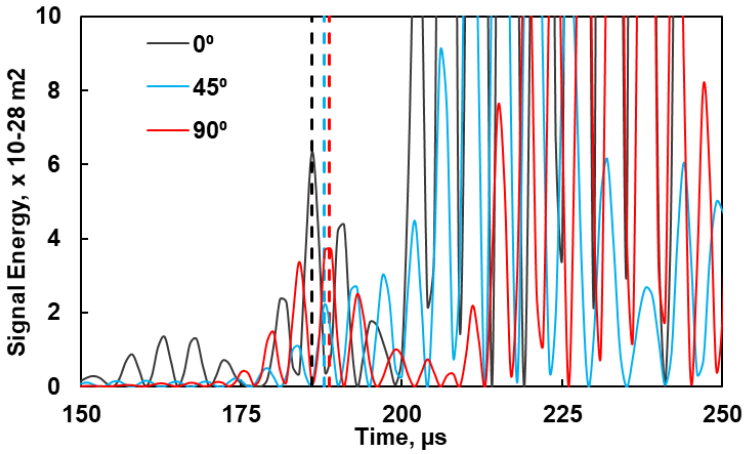

Figure 4.18 Variations in signal energy with respect to the orientation of the embedded PZT cement modules from the FE analysis

4.3.3 Comparison of Experimental and Numerical Results

The comparisons of the ToF and WMoE were based on the results of the numerical analysis and experimental investigation at 28 days. The same central frequency and material properties from the material tests were used as inputs to the numerical simulation. In particular, the SMoE of the concrete at 28 days, 24.1 GPa, was used as the input for the numerical FE analysis. The data from the numerical FE simulation were analyzed in the same way as described for the experimental investigation. The ToF values of the first S-wave package for the embedded PZT cement module system obtained from the numerical and experimental investigations were first compared. As illustrated in figure 4.19, the ToF approximations were very close, regardless of the orientation of the PZT cement modules. As no damping boundaries were used in the FE simulation, these approximations to the actual scenario were acceptable. B#1 (with $\theta = 0^o$ orientation of the embedded PZT cement modules) and B#3 (with $\theta = 90^o$ orientation of the embedded PZT cement modules) had the same ToF values in both the numerical and experimental results. In contrast, the numerically predicted ToF for B#2 ($\theta = 45^o$ orientation) varied only 1.5 percent from the experimentally measured ToF in the smart PZT cement module system. Therefore, the

experimental measurements of the WMoE based on the embedded PZT cement module system were consistently validated by the FE model.

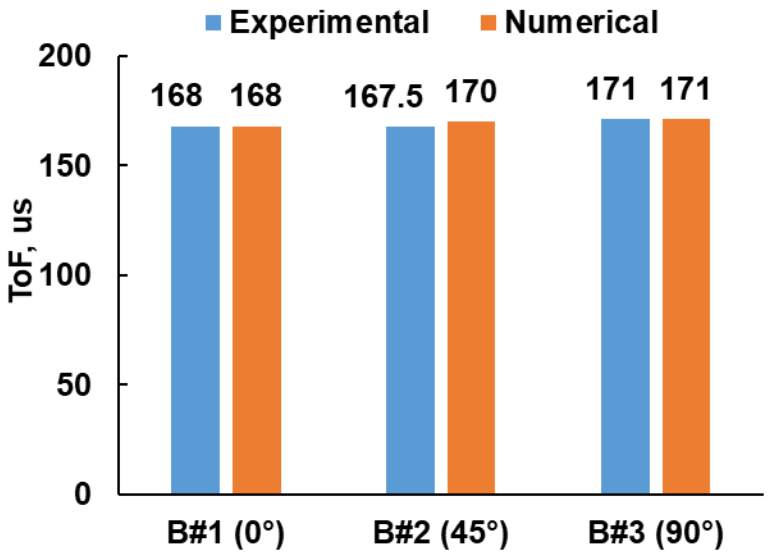

Figure 4.19 Comparison of the ToF values of the first S-wave package between the experimental and numerical results from beams at 28 days

The variations in the ToF values of the first R-wave package for the surface-mounted PZT patch system between the numerical FE analysis and experimental investigation are shown in figure 4.20. The orientation effect was not a concern for the surface-mounted PZT patches, and the ToF values for three beams from the numerical analysis were the same (i.e., 186 μs) because the same geometry and material properties were given. Therefore, the beams were named B#1, B#2 and B#3, primarily for the experimental measurements. The experimental measurements based on the surface-mounted PZT patch system were also successfully validated by the FE model. The numerically predicted ToF was slightly higher than all the ToF values from the three experimental beam investigations. The variations in ToF values for the surface-mounted PZT patches between the numerical simulation and the experimental investigations were approximately 2.76 percent for B#1, 2.48 percent for B#2, and 0.81 percent B#3.

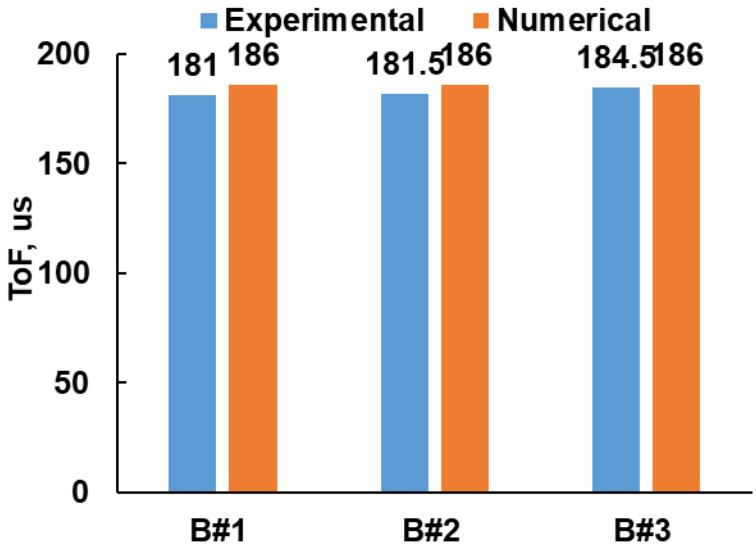

Figure 4.20 Comparison of the ToF values of the first R-wave package from the surface-mounted PZT patches at 28 days between the experimental and numerical results

The WMoE data from the experimental investigation and numerical analysis of the two PZT system measurements at 28 days are summarized in table 4.3 and plotted in figure 4.21. Obviously, the SMoE (i.e., 24.14 GPa at 28 days, see table 4.1), measured in accordance with ASTM C469, was always lower than all experimentally measured and numerically predicted WMoE values.

As discussed before, there were some differences between the WMoE values determined by the surface-mounted PZT patches and the embedded PZT cement modules because of the variation in the hydration rate between the exterior and interior of the concrete. After 28 days, the variations between those two measurements were approximately 3.7 percent, 2.5 percent, and 3.4 percent, respectively. Similarly, the numerically predicted WMoE data from the surface-mounted PZT patches and the embedded PZT cement modules also exhibited some variation. The WMoE determined by the FE model was 25.3 GPa for the surface-mounted PZT patches. The WMoE values determined by the FE model for the embedded PZT cement modules were 25.81 GPa for

B#1, 25.21 GPa for B#2, and 24.91 GPa for B#3. The corresponding variations between the two systems produced by the FE models were 2.0 percent for B#1, 0.35 percent for B#2, and 1.5 percent for B#3. The WMoE and variation values were more consistent with each other, indicating that the effects of the embedded orientation were not as great in the FE model as in the experimental evaluation. It is reasonable that the location and orientation of the PZT, as well as the input of material properties, were more easily controlled in the FE analysis.

To validate the accuracy of the test results of both the embedded and surface-mounted PZT measurement systems, the experimentally measured and numerically predicted results were compared in terms of WMoE values. For the embedded PZT cement modules, the WMoE values for B#1 and B#3 from the experimental and numerical methods were the same because of the same ToF value, whereas the experimentally measured WMoE from B#2 was approximately 3.0 percent higher than the numerically predicted value. The coefficient of variation (COV) of the experimental investigation using the different orientations of the embedded PZT cement modules was 2.22 percent, while the numerical investigation produced a COV of 1.81 percent. The WMoE results for the surface-mounted PZT patches from the experimental measurements were always higher than the numerically predicted values. The differences between the experimentally measured and numerically predicted results were relatively high for B#1 (5.73 percent) and B#2 (5.13 percent) and were low for B#3 (1.74 percent).

Table 4.3 Comparisons of experimentally measured and numerically predicted WMoE values

Beam	Embedded PZT			Surface-mounted PZT		
	Experimental (GPa)	Numerical (GPa)	Difference (%)	Experimental (GPa)	Numerical (GPa)	Difference (%)
B#1	25.81	25.81	0	26.75	25.30	5.73
B#2	25.96	25.21	2.98	26.60	25.30	5.13
B#3	24.91	24.91	0	25.74	25.30	1.74

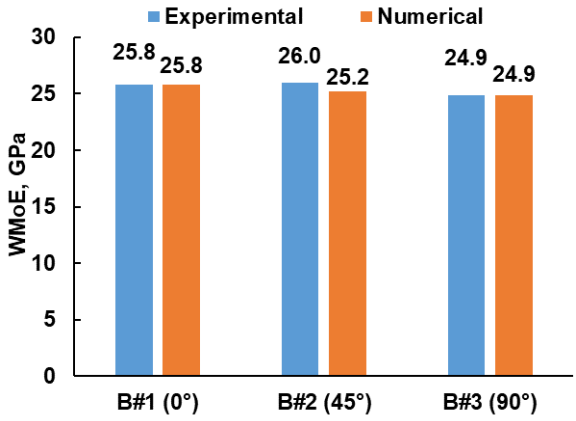

(a) Embedded PZT cement module system

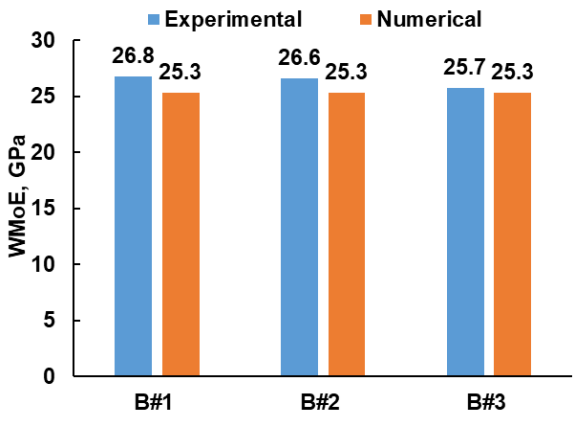

(b) Surface-mounted PZT patch system

Figure 4.21 Comparison of experimentally measured and numerically predicted WMoE values

4.4 Results from the Experimental Investigation of the Concrete Panel

The experimental results obtained from the arrays of embedded smart PZT cement modules and the surface-mounted PZT patches on the concrete panel up to 28 days are illustrated in figures 4.22 and 4.23, respectively. Because the wave patterns were like those of the experimental investigations of the concrete beam samples, the details are not provided. Note that the results from the embedded modules E-B and E-D were discarded, because the response signals from those two PZT cement modules were too noisy (for undetermined reasons), and it was quite difficult to obtain the peak of the first S-wave package.

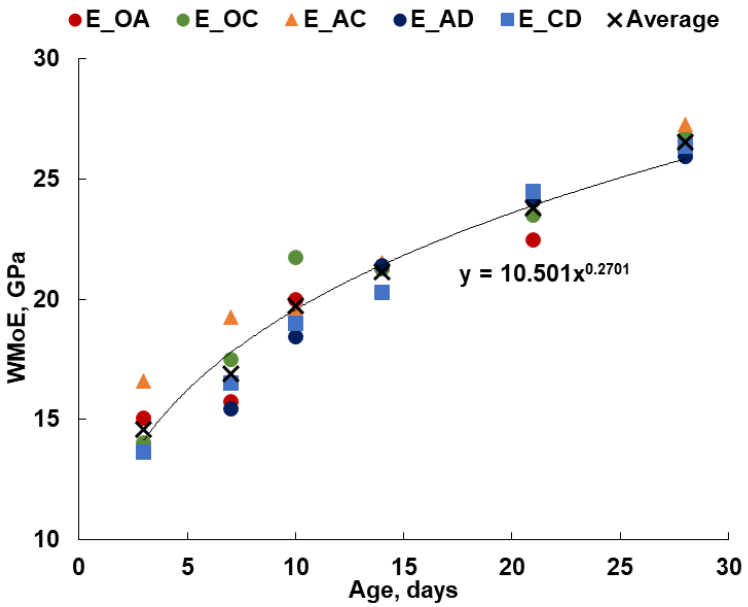

Figure 4.22 Measured WMoE over time from the embedded cement module system

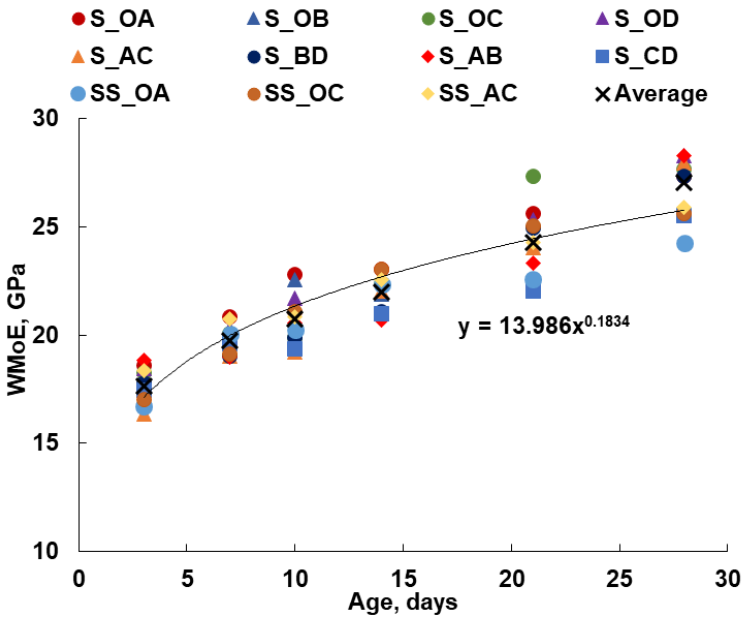

Figure 4.23 Measured WMoE over time from the surface-mounted PZT patch system

4.4.1 PZT Placement Effects

To get a better understanding of the effects of PZT placement (i.e., embedded vs surface-mounted) on the variations in estimated WMoE values when the distance between each PZT

actuator-sensor pair was the same, the corresponding WMoE results at 28 days for the embedded PZT cement module system (E-labelled), surface-mounted PZT patches (S-labelled), and side surface-mounted PZT patches (SS-labelled) were compared and are depicted in figure 4.24. At the 28th day after the concrete beam had been cast, the SS-labelled PZT patches and embedded PZT cement modules (E)varied by 8.1 percent for a separation distance of 175 mm between the PZT sensor and actuator pairs and by 5.0 percent for a separation distance of 350 mm. The corresponding variations for the S-labelled PZT patches in comparison to the embedded PZT cement modules were values 3.5 percent higher for a separation distance of 175 mm between the PZT sensor and the actuator pairs, 3.5 percent higher for a distance of 248 mm, and 2.6 percent higher for 350 mm. Overall, at the short distance of 175 mm (OA), the estimations of the WMoE for the surface-mounted PZT patches on the square surface (PZTs with suffix S) tended to be higher than those for the embedded PZT cement module (E)and side surface (SS)-mounted PZT patches. However, there were no clear patterns for a distance of 248 mm (CD). For the longest distance of 350 mm (AC), the estimations of the WMoE were very similar.

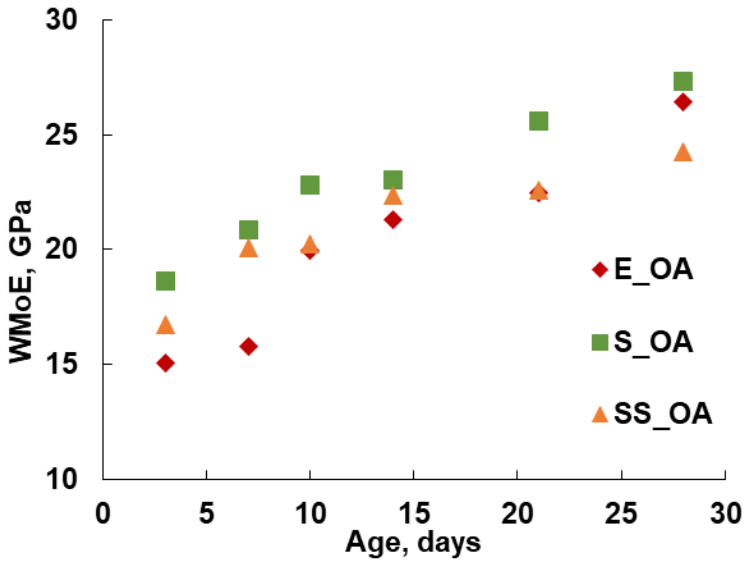

(a) Distance OA = 175 mm

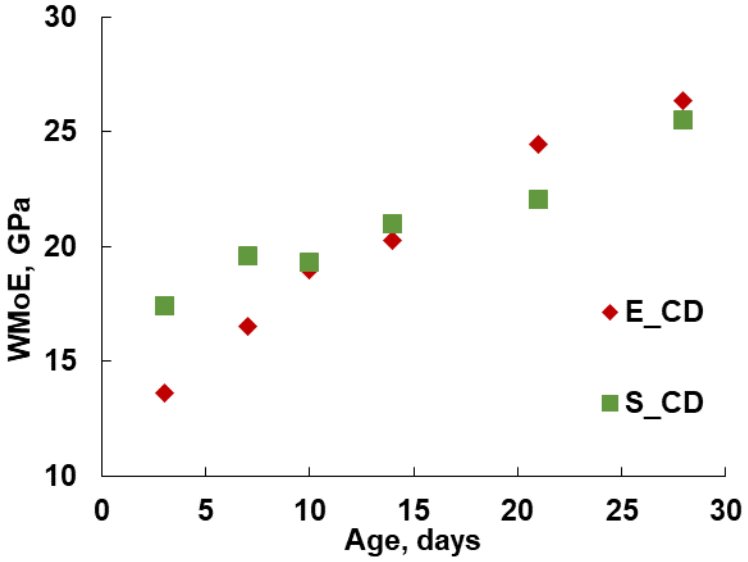

(b) Distance CD = 248 mm

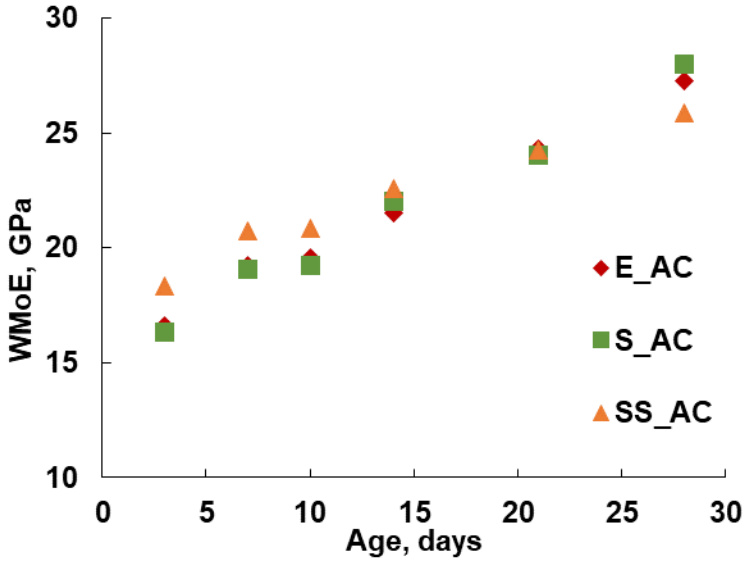

(c) Distance AC = 350 mm

Figure 4.24 Comparison of estimated WMoE values obtained for the embedded PZT cement modules (E), surface-mounted PZT patches (S), and side surface-mounted PZT patches (SS)

4.4.2 Distance Effects

To understand the effects of the distance of the PZT sensor-actuator pair, the experimentally measured WMoE for the embedded PZT cement modules (E-labelled), surface-mounted PZT patches on top surface (S-labelled), and side surface-mounted PZT patches (SS-labelled) were compared and are shown in figures 4.19 to 4.21, respectively. As shown in figures 4.19 to 4.21, the effects of the distance between the PZT actuator and sensor among three cases were small, and there was no clear relationship between the distance of the PZT actuator-sensor pair and the measured WMoE. However, the distance between the sensor-actuator pair affected the clarity of the wave signal. As the distance increased, the amplitude of the wave signal correspondingly decreased, indicating that the PZT actuator-sensor pair for determining WMoE should not be placed too far away from each other.

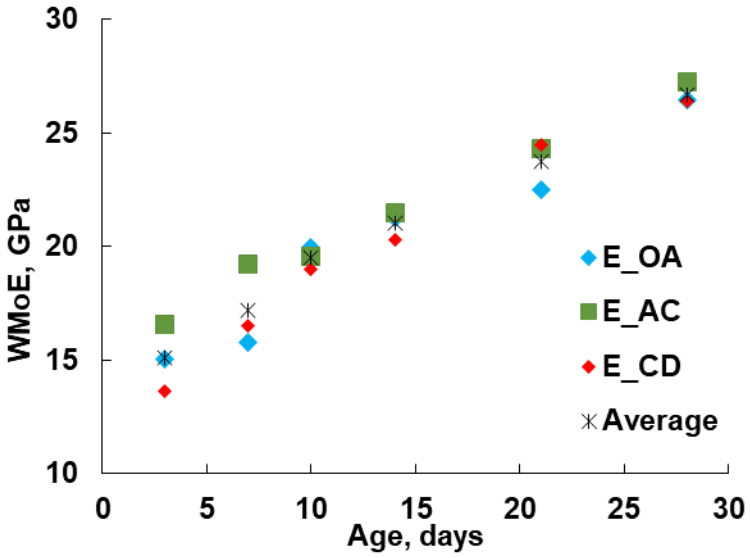

Figure 4.25 Variation of estimated WMoE from the embedded PZT cement modules with various distances: OA = 175 mm, CD = 248 mm, AC = 350 mm

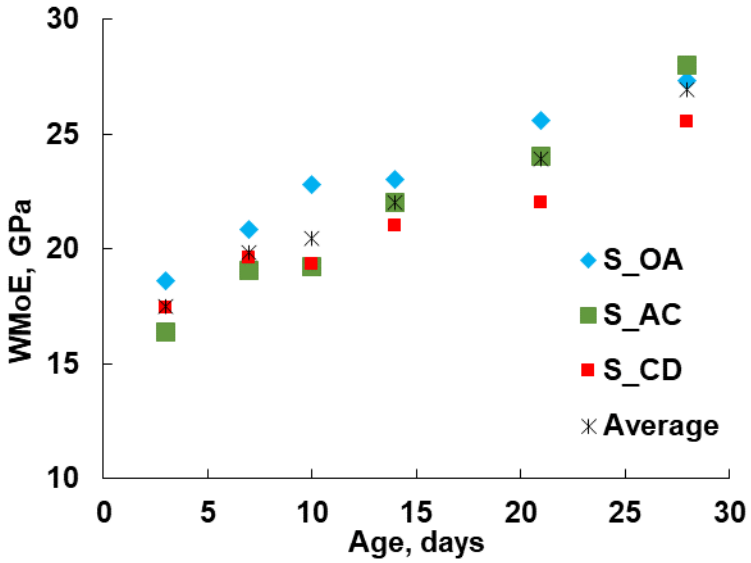

Figure 4.26 Variation of estimated WMoE from the surface-mounted PZT patches with various distances: OA = 175 mm, AB = 248 mm, AC = 350 mm

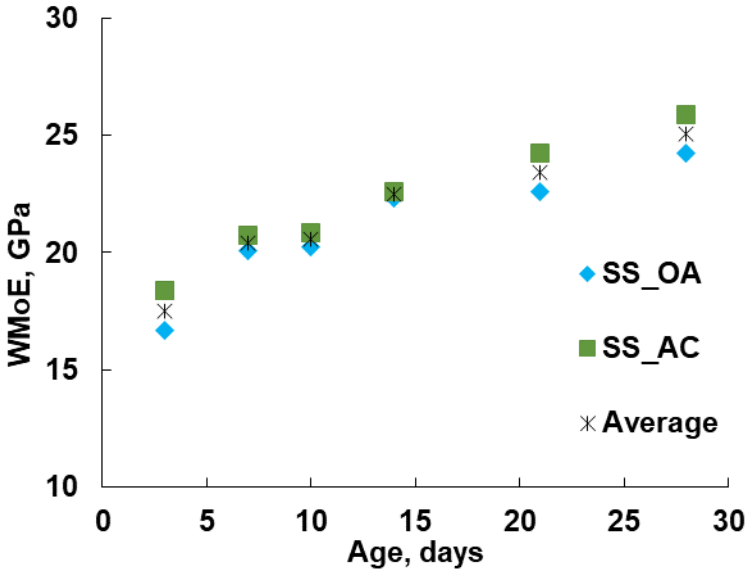

Figure 4.27 Variation of estimated WMoE from side surface-mounted PZT patches with various distances: OA = 175 mm, AC = 350 mm

4.5 Discussion of "Embedded PZT Cement Module System" versus "Surface-Mounted PZT Patch System"

The WMoE determined with the embedded PZT cement module system and surface-mounted PZT patch system from each case of concrete beams and concrete panel are summarized in table 4.4 and shown in figure 4.22. The WMoE values determined from the surface-mounted PZT patches tended to be slightly higher than those from the embedded PZT cement module. Using the surface-mounted PZT patches, the average WMoE values for the concrete panel in comparison to those for concrete beams varied by 3.9 percent at 7 days, 1.4 percent at 14 days, and -3.8 percent at , 28 days. Using the embedded PZT cement modules, the WMoE values for the concrete panel in comparison to those for the concrete beams were -0.5 percent at 7 days, -6.4 percent at 14 days and -4.4 percent at 28 days. The differences in curing age may have contributed to the slight variations of the results. The hydration rates of cementitious materials at different depths may exhibit some differences; concrete exterior surfaces gain strength and stiffness more quickly than the interior, which resulted in some variations between interior and exterior WMoE values. As discussed, the surface-mounted PZT patch measurement system is better related to concrete surface properties within one wavelength of depth, while the embedded PZT cement module system is more relevant to the interior property measurement of concrete. At 7 days, regardless of concrete dimension effect (either beam or panel), the measured WMoE from the surface-mounted PZT as approximately 14.6 percent higher than that from embedded PZT cement modules. After 14 days, this variation decreased to approximately 6.0 percent. At 28 days, this variation decreased to approximately 3.4 percent, indicating that the interior and exterior of the concrete had fully cured. Overall, the surface-bonded PZT system was as effective as or even better than the embedded PZT cement module system in determining WMoE because it provided comparable WMoE results and is more effective for installation on existing structures.

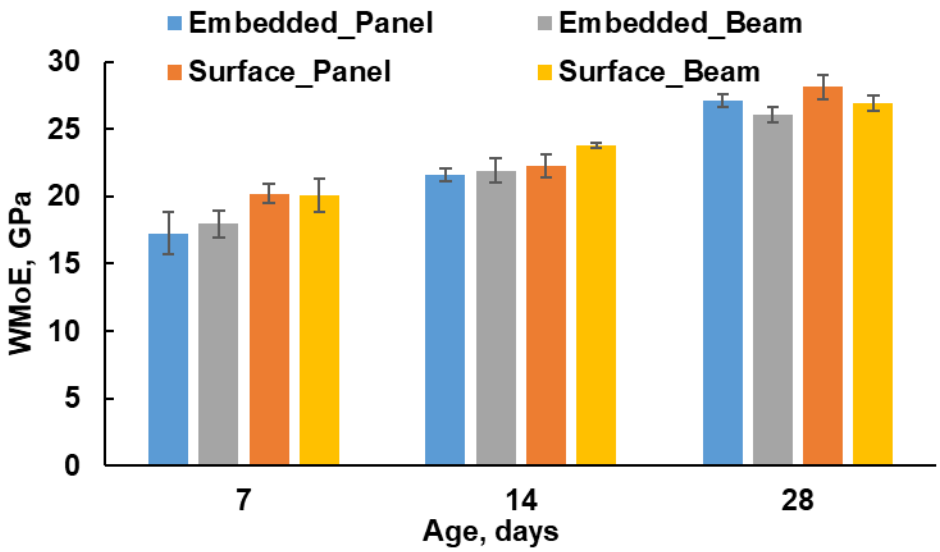

Figure 4.28 Comparison of WMoE results for concrete beams and panel

Table 4.4 WMoE of the concrete beams and panel experimentally determined by two smart PZT systems

Concrete Age (days)		7	14	28
Embedded PZT	Panel (GPa)	17.2	21.6	27.1
	Beams (GPa)	18.0	21.9	26.1
Surface-mounted PZT	Panel (GPa)	20.2	22.3	28.1
	Beams (GPa)	20.1	23.8	26.9

Chapter 5 Conclusions and Recommendations

5.1 Conclusions

This study aimed to develop a surface-mounted PZT patch system and embedded PZT cement module system to determining of the wave modulus of elasticity (WMoE) of concrete structures. A combined experimental and numerical study was conducted using both the PZT systems to determine the WMoE of concrete. The effects of the orientation of the embedded PZT cement modules on propagating waves were also investigated, and the feasibility of using the surface-mounted PZT patches on a narrower structure with a greater depth was also explored. The observations and findings from the combined experimental and numerical investigation are summarized as follows.

- The propagating shear wave (S-wave) from the excitation signal was chosen for determining the WMoE of concrete beams using embedded smart PZT cement modules. The orientation of the embedded PZT cement modules influencds the clarity and the magnitude of the propagating waves. At the orientation of 90º, the propagating wave overlapped with the reflective wave, and the wave peak shifted to the right, prolonging the time of flight (ToF) and ultimately resulting in a lower WMoE. The response signal from the embedded PZT cement modules oriented at 45º incorporated some noise, while the ones oriented at 0º produced the best response signal. Though the orientation affected the clarity and magnitude of the propagating wave, there was not too much difference among the experimentally measured WMoE values.
- The propagating Rayleigh wave (R-wave) from the excitation signal was selected for determining the WMoE of concrete beams using the surface-mounted PZT patch system. The surface-mounted PZT patch system resulted in higher WMoE values than the

embedded smart PZT cement module system. The maximum difference between the two systems was only 3.3 percent at 28 days.

- A numerical finite element (FE) model was established by using an input static modulus of elasticity (SMoE) of concrete of 24.1 GPa as experimentally measured from the compression test. The WMoE values predicted by the numerical FE model varied depending on the orientation of the embedded smart PZT cement modules. The numerically predicted WMoE values were 25.81 GPa at a 0º orientation of the embedded smart PZT cement module, 25.21 GPa at 45º, and 24.91 GPa at 90º, while the numerically predicted WMoE value was 25.3 GPa for the surface-mounted PZT patch system. Because of the dynamic effect, all the numerically predicted WMoE values for the embedded or surface-mounted PZT were higher than the input SMoE.
- The WMoE results from the experimental measurement at 28 days were the same as or higher than those from the numerical prediction, with a maximum variation of 3.7 percent. The accuracy of the experimentally measured WMoE results for both the smart PZT systems was thus validated by the numerical FE model.
- The surface-mounted PZT patches were better for measuring the concrete within one wavelength of depth from the surface, whereas the PZT cement modules embedded in concrete structures evaluated the interior properties of the concrete. The R-wave from the surface-mounted PZT patch system only propagated within one wavelength of depth from the surface, and the resulting WMoE values did not necessarily represent the measured WMoE of the interior of the concrete structures.
- A concrete panel was cast and evaluated to potentially implement the PZT systems in real concrete structures. The distance of the PZT actuator-sensor pair slightly influenced the

estimated WMoE, but no clear relationship was observed. The WMoE value obtained from the embedded PZT cement module system was lower by 3.5 percent than that from the surface-mounted PZT patch system with an actuator-sensor pair distance of 175 mm, lower by 3.4 percent at a distance of 248 mm, and lower by 2.6 percent at a distance of 350 mm. The estimated WMoE values from the PZT actuator-sensor pairs mounted on the narrower surface with a larger depth were higher than values from the PZT pairs mounted to the wider surface by 8.1 percent with an actuator-sensor pair distance of 175 mm and by 5.0 percent with a distance of 350 mm. Although the effect of the distance of the PZT actuator-sensor pair was not significant for determining the WMoE, the amplitude of the wave signal decreased as the distance increased, thus affecting the discretion of the peak response signal and creating difficulty in determining the ToF.

In summary, the surface-bonded PZT patch system is as effective as or even better than the embedded PZT cement module system in determining the WMoE of concrete with a certain degree of confidence, and both the smart PZT systems are capable of assessing the condition of concrete structures by evaluating WMoE changes over time and/or under different loading and conditions. The surface-mounted PZT patch system has more advantages in terms of easy and accurate installation and placement on existing concrete structures because the PZT patches can be nondestructively surface-mounted to the concrete structures. Therefore, it is a promising alternative nondestructive and condition assessment technique for concrete structures. However, the surface-mounted PZT patch system only represents the WMoE measurement of concrete structures within one wave length of depth from the surface.

5.2 Recommendations

Because only the WMoE values of concrete produced by both the embedded and surface-mounted PZT systems were determined and compared in this study, additional investigations of both systems should be performed to identify the presence of cracks, different types of concrete material damage and degradation, and more. Investigation of the application of both systems for implementation in large-scale civil infrastructure should be expanded. In addition, the extension of the techniques for monitoring and detection of reinforced concrete structures (e.g., detecting corroded reinforcing bars in concrete) should be explored.

References

ASTM C138/C138M-16a. 2016. Standard Test Method for Density (Unit Weight), Yield, and Air Content (Gravimetric) of Concrete. ASTM International, West Conshohocken, PA.

ASTM C143/C143M-15a. 2015. Test Method for Slump of Hydraulic-Cement Concrete. ASTM International, West Conshohocken, PA.

ASTM C39/C39M-16. 2016. Standard Test Method for Compressive Strength of Cylindrical Concrete Specimens. ASTM International, West Conshohocken, PA.

ASTM C469/C469M-14. 2014. Standard Test Method for Static Modulus of Elasticity and Poisson's Ratio of Concrete in Compression. ASTM International, West Conshohocken, PA.

Bhalla, Suresh, Sumedha Moharana, Visalakshi Talakokula, and Kaur Naveet. 2017. Piezoelectric Materials: Applications in SHM, Enrgy Harvesting and Bio-mechanics. John Wiley & Sons Ltd.

Cady, W.G., 1946. Piezoelectricity: An introduction to the theory and applications of Electromechanical Phenomena in Crystals, International Series in Pure and Applied Physics. McGraw-Hill Book Company, Inc.

Curie, J., Curie, P., 1880. Development, via compression, of electric polarization in hemihedral crystals with inclined faces. Bull. Soc. Minerol. Fr. 3, 90–93.

Drozdz, M.B., 2008. Efficient Finite Element Modelling of Ultrasonic Waves in Elastic Media. Imperial College, University of London.

Giurgiutiu, V., 2008. Structural Health Monitoring with piezoelectric wafer active sensors. Elsevier Inc.

Gu, H., Song, G., Dhonde, H., Mo, Y.L., Yan, S., 2006. Concrete early-age strength monitoring using embedded piezoelectric transducers. Smart Mater. Struct. 15, 1837–1845.

Hu, B., Kundu, T., Grill, W., Liu, B., Toufigh, V., 2013. Embedded Piezoelectric Sensors for Health Monitoring of Concrete Structures. ACI Mater. J. 110, 149–158.

Ikeda, T., 1990. Fundamentals of Piezoelectricity. Oxford University Press.

Jordan, T.L., Ounaies, Z., 2011. Piezoelectric Ceramics Characterization (No. ICASE Report No. 2001-28). Institute for Computer Applications in Science and Engineering, Hampton, Virginia.

Li, W., Kong, Q., Ho, S.C.M., Lim, I., Mo, Y.L., Song, G., 2016. Feasibility study of using smart aggregates as embedded acoustic emission sensors for health monitoring of concrete structures. Smart Mater. Struct. 25, 115031.

Lim, Y.Y., Kwong, K.Z., Liew, W.Y.H., Soh, C.K., 2016. Non-destructive concrete strength evaluation using smart piezoelectric transducer - a comparative study. Smart Mater. Struct. 25, 085021.

Lippman, G., 1881. Principal of the conservation of electricity. Ann. Chem. Phys. 24, 145.

Liu, T., Huang, Y., Zou, D., Teng, J., Li, B., 2013. Exploratory study on water seepage monitoring of concrete structures using piezoceramic based smart aggregates. Smart Mater. Struct., 065002 22, 8pp.

Markovic, N., Nestrorovic, T., Stojic, D., 2015. Numerical modeling of damage detection in concrete beams using piezoelectric patches. Mech. Res. Commun. 64, 15–22.

Moslehy, Y., Gu, H., Belarbi, A., Mo, Y.L., Song, G., 2010. Smart aggregate based damage detection of circular RC columns under cyclic combined loading. Smart Mater. Struct. 19, 12pp.

Qiao, P., Fan, W., Chen, F., 2011. Material Property assessment and crack identification of recycled concrete with embedded smart cement modules, in: Proc. SPIE 7981. Presented at the Sensors and Smart Structures Technologies for Civil, Mechanical, and Aerospace systems 2011, p. 79814V.

Rehman, S.K.U., Ibrahim, Z., Memon, S.A., Jameel, M., 2016. Nondestructive test methods for concrete bridges : A review. Constr. Build. Mater. 107, 58–86.

Rose, J.L., 1999. Ultrasonic Waves in Solid Media. Cambridge University Press, Cambridge, United Kingdom.

Shirohi, J., Chopra, I., 2000. Fundamental understanding of Piezoelectric Strain Sensors. J. Intel. Mater. Syst. Struct. 11, 246–257.

Song, G., Gu, H., Mo, Y.-L., 2008. Smart aggregates: multi-functional sensors for concrete structures - a tutorial and a review. 17 033001.

Song, G., Huang, G.L., Kim, J.H., Haran, S., 2008. On the study of surface wave propagation in concrete structures using a piezoelectric actuator/sensor system. Smart Mater. Struct. 17, 055024.

Sun, M., Staszewski, W.J., Swamy, R.N., Li, Z., 2008. Application of low-profile piezoceramic transducers for health monitoring of concrete structures. NDTE Int. 41, 589–595.

Tseng, K.K., Wang, L., 2014. Smart piezoelectric transducers for in situ health monitoring of concrete. Smart Mater. Struct. 13, 1017–1024.

Yan, S., Sun, W., Song, G., Gu, H., Huo, L.-S., Liu, B., Zhang, Y.-G., 2009. Health Monitoring of Reinforced concrete shear walls using smart aggregates. Smart Mater. Struct. 18.